Master's thesis

NTNU
Norwegian University of Science and Technology
Faculty of Engineering
Department of Energy and Process Engineering

Sanne de Jong Helvig

A comparison of lab-scale free rotating wind turbines and actuator disks

Master's thesis in Energy and Environmental Engineering
Supervisor: Nicholas Worth, R. Jason Hearst, Magnus Kyrkjebø Vinnes
June 2020

NTNU
Norwegian University of
Science and Technology

Sanne de Jong Helvig

A comparison of lab-scale free rotating wind turbines and actuator disks

Master's thesis in Energy and Environmental Engineering
Supervisor: Nicholas Worth, R. Jason Hearst, Magnus Kyrkjebø Vinnes
June 2020

Norwegian University of Science and Technology
Faculty of Engineering
Department of Energy and Process Engineering

NTNU
Norwegian University of
Science and Technology

Preface

This thesis is the conclusion of my Master of Science within Energy and Environmental Engineering at the Norwegian University of Science and Technology, where I chose to specialize in Energy and Process Engineering. The work that has gone into this thesis has often been challenging, yet always exciting. It has provided me with in-depth theoretical and experimental knowledge, and I am happy that I can bring this new knowledge and these new skills with me into my future work.

I would like to thank my supervisor Nicholas Worth and my co-supervisor Jason R. Hearst for all their help and support along the way. They provided me with all the guidance I needed, despite the difficulties arising from the COVID-19 pandemic. I also want to give my sincere thanks to Magnus Kyrkjebø Vinnes, for helping me out whenever I had problems and for always being available when I needed input. I have learned so much from him. Further, I want to thank Antonio Segalini for his help with improving my paper. I would like to show my appreciation to the Ph.D. students at the Department of Energy and Process Engineering who have helped me out with heavy lifting and given me useful input at our group meetings. Finally, I would like to thank Adrian Bogen Skibelid, for proofreading, programming advice, and his continuous support.

Sanne Helvig

Trondheim, 10.juni 2020

Problem description

The following is a shortened version of the master's agreement that was written by the supervisors, describing the master's project.

Actuator disks are a commonly used substitute for rotating blade wind turbines because they significantly simplify the system. Actuator disks are employed in both simulations and experiments. Static actuator disks are both easier to simulate in the computer and to manufacture en masse for experiments. However, actuator disks are typically designed to match the drag produced by a wind turbine, and this does not guarantee the flow fields or instantaneous phenomena are the same. This has consequences when actuator disks are used to make predictions for full scale wind farm installations. For instance, an issue that has recently come to prominence for wind farms is their "blockage effect" as a whole on the flow entering the farm. In particular, how the presence of the farm effects the upstream flow. Estimates of these effects with actuator disks appear to be inconsistent with field measurements. As such, the present project focuses on performing detailed flow field measurements on the upstream effects of a wind farm of both rotating wind turbines and static actuator disks.

The following tasks will be completed in this project:

1. Select a suitable actuator disk with matched drag to the rotating turbines.
2. Determine two farm layouts.
3. Create a platform to mount the wind farms to the wind tunnel floor.
4. Prepare the wind tunnel for Particle Image Velocimetry (PIV) measurements.
5. Create and measure two different incoming flows to the wind farm.
6. Measure the flow field immediately upstream of the wind farm and over the first few turbines for all eight configurations (two types of turbines, two layouts, two incoming profiles).
7. Repeat the above measurements with the wind farm rotated to a couple of suitable angles.
8. Convert all PIV images into vector fields and at a minimum compare first- and second-order statistics across the cases, with consideration of the impact of the non-rotating wakes on the differences or similarities between the results.
9. Prepare a final report in journal format detailing the findings of the study.

Due to the COVID-19 situation, laboratory work was suspended at EPT indefinitely on Thursday 12th March 2020. Therefore, the candidate should not be penalised for incomplete tasks in the above list, but should retain credit for completed work towards these. In agreement with recommendations made by EPT, the following ammendments have been made to the list of proposed tasks for this Masters project.

1. Report on activities and plans prior to the lab closure on March 12th.

Further to this task, the candidate is requested to follow a revised objective, which is the data processing and analysis of a previously obtained experimental data set. This data set contains statistically resolved PIV measurements of a spinning rotor, and a number of actuator disks of varying design. The following new tasks are to be considered:

2. Process vector fields and compare first- and second-order statistics across the cases, with consideration of the impact of the non-rotating wakes on the differences or similarities between the results.

3. An investigation of Proper Orthogonal Decomposition (POD) as an analysis method for highlighting the wake dynamics of different cases.

4. Prepare a final report in journal format detailing the findings of the study.

Sammendrag

Planar particle image velocimetry ble gjennomført oppstrøms og i den nærliggende vaken til en roterende vindturbinmodell i laboratorieskala og aktuatordisker av samme dimensjon i en vindtunell. Den innkommende strømningen hadde et Reynolds tall i størrelsesorden 10^4. Aktuatordisker med ulike design og soliditeter ble testet, og prosessen med å velge aktuatordisk er vist. Den resulterende luftmotstanden, gjennomsnittlig hastighet og gjennomsnittlig *vorticity* i vaken til diskene ble sammenlignet med tilsvarende størrelser for den roterende modellen. Den disken med vake som mest nøyaktig gjenskapte vaken til den roterende modellen ble så studert i mer detalj. *Reynolds stresses* ble sett på for å fastslå at de gjennomsnittlige karakteristikkene i strømningene sammenfalt. På tross av sammenlignbare gjennomsnittsfelt viste en analyse av *instantaneous swirling strength* at det var betydelige forskjeller mellom de momentane fenomenene i strømningene. Distinkte *tip vortices* var til stede i vaken til den roterende modellen, men var fraværende i vaken til aktuatordisken. I tillegg var *swirl* av høy intensitet til stede direkte nedstrøms for aktuatordisken, forårsaket av turbulent miksing av strømningsstråler som passerer gjennom disken. Tilsvarende fenomen var ikke til stede bak de roterende turbinbladene. *Proper orthogonal decomposition* ble brukt for å videre studere de underliggende fenomenene i de to strømningene. Også denne analysen viste viktigheten av *tip vortices* når man studerer den roterende modellen og mangelen på slike distinkte *vortices* når man bruker aktuatordisken. Dermed, på tross av lignende gjennomsnittlige karakteristikker, forblir de momentane strukturene i de to strømningene ulike.

A comparison of lab-scale free rotating wind turbines and actuator disks

Sanne de Jong Helvig[a], Magnus Kyrkjebø Vinnes[a], Antonio Segalini[b], Nicholas Worth[a] and R. Jason Hearst[a,*]

[a]Department of Energy & Process Engineering, Norwegian University of Science & Technology, NO-7491, Trondheim, Norway
[b]Linné Flow Centre, STandUP for Wind, KTH Mechanics, Stockholm, Sweden

ARTICLE INFO

Keywords:
Wind turbine
Actuator disk
Lab-scale
POD

ABSTRACT

Planar particle image velocimetry was conducted upstream and in the near-wake of a lab-scale rotating wind turbine model and actuator disks of the same dimensions in a wind tunnel, at an incoming flow Reynolds number of the order 10^4. Actuator disks with different designs and solidities were tested, and the process of actuator disk selection is shown. The produced drag, mean velocity and mean vorticity in the wake of the disks were compared to that of the rotating model. The disk whose wake most closely replicated the wake of the rotating model was then studied in more detail, analyzing mean Reynolds stresses to determine that the mean characteristics of the flows were similar. However, the instantaneous swirling strength illustrated that despite similar mean fields, the instantaneous phenomena were significantly different. Distinct tip vortices were present in the wake of the rotating model, but were absent from the wake of the actuator disk. Furthermore, high intensity swirl was present directly downstream of the actuator disk, caused by turbulent mixing of jets passing through the disk, which was not present behind the rotating turbine blades. Proper orthogonal decomposition was used to further study the underlying phenomena in the two flows, again demonstrating the importance of tip vortices when studying the rotating model and the lack of such distinct vortices when using the actuator disk. Hence, despite similar mean characteristics, the instantaneous structures in the two flows remain distinct.

1. Introduction

Renewable energy now accounts for a third of global power capacity, and, according to Siemens (2019), wind power alone may represent one third of the global electric demand by 2040. Placing wind turbines in wind farms is the most economic and efficient implementation with respect to planning, maintenance and use of land and infrastructure. However, it means that the turbines are permanently exposed to the wakes caused by upstream rows of turbines, and hence, Veers et al. (2019) stated that the first grand challenge in wind energy research today is improved understanding of wind farm flow physics. Porté-Agel et al. (2019) also described the importance of further developing models for wind farm wake flow studies and extending these studies to include factors such as topography, thermal stability and the role of atmospheric turbulence.

Field tests of wind farms have been and continue to be carried out (Barthelmie and Jensen, 2010; Smith et al., 2013; Barthelmie et al., 2015; Zhan et al., 2019, 2020), but such approaches are expensive, difficult and, by their nature, incapable of being completely controlled, unlike lab-scale experiments. Using small-scale models makes it possible to study wind farms in a wind tunnel. Lab-scale experiments are thus helpful in providing a deeper understanding of large scale physics at a range of different conditions, e.g., different incoming flow velocities and turbulence levels. Multiple small-scale wind farm experiments have already been performed (Theunissen et al., 2014; Camp and Cal, 2016; Bossuyt et al., 2017; Camp and Cal, 2019; Segalini and Dahlberg, 2020), providing new knowledge of wind farm flows and how to improve wind farm efficiency (Stevens and Meneveau, 2017). However, the complexity of constructing and using numerous rotating turbine models is challenging, which is why, on occasion, simplifications are sought.

The actuator disk is a common simplification of a rotating blade, horizontal-axis wind turbine, used both in experiments and simulations. The simple structure of a static actuator disk is easier to simulate than the blades of a moving rotor, allowing for fewer grid cells, which can have larger dimensions, and hence allowing for larger time steps. In turn, the simulations are not as computationally intensive. Stevens and Meneveau (2014) used actuator disks in simulations to study the effect of wind-input variability on wind farm power fluctuations. Later, Stevens et al. (2014) used actuator disks when simulating and studying row alignment in wind farms. Wu and Porté-Agel (2012) used actuator disk simulations to study atmospheric turbulence effects on wind turbine wakes. Work has been done on testing and further developing the actuator disk as a simulation tool, and comparing the simulations to experimental results (Harrison et al., 2010; Wu and Porté-Agel, 2011; Martínez Tossas et al., 2014; Lignarolo et al., 2016a; Simisiroglou et al., 2017). Static actuator disks are also easier and less costly to manufacture en masse for use in experiments, and often more robust than using moving parts. Blackmore et al. (2013) used actuator disks as a simplification for tidal turbines to study the effect of turbulence on drag force in a water current. Howland et al. (2016) examined the deflection and morphology of wakes behind an actuator disk model of a wind turbine operating in yawed conditions. Bossuyt et al. (2017) used actuator disks to model different wind farm layouts to examine unsteady loading. Theunissen et al. (2014) con-

*Corresponding author.
jason.hearst@ntnu.no (R.J. Hearst)
ORCID(s): 0000-0003-2002-8644 (R.J. Hearst)

ducted actuator disk wind farm experiments as a validation, and possible source of improvement, of the actuator disk as a computational tool. While the actuator disk is shown to be a common and convenient simplification, how well actuator disks replicate the behavior of rotating turbines, and how much of an influence the actuator disk geometry has, is still being established.

Actuator disks are typically designed to resemble a specific rotating wind turbine, by matching the diameter of the disk with the diameter of the rotor, and by matching the drag coefficient (sometimes referred to as the "thrust coefficient" in wind turbine literature). Besides that, there are to date no standards in terms of actuator disk design and production. Camp and Cal (2016, 2019), Bossuyt et al. (2017) and Neunaber (2018) used designs with a solidity that decreases with radial coordinate. Aubrun et al. (2013), and later Lignarolo et al. (2014, 2016b), used fine metal meshes with varying porosity at the center of the disc and the outer edge. Blackmore et al. (2013) used a pattern of circular, equally sized holes to maintain approximately uniform porosity across the radius. Sforza et al. (1981) made their actuator disks from perforated metal plates, while Pierella and Sætran (2010) used wooden grids, and Myers and Bahaj (2010) used thin sheets of PVC plastic to create mesh disks. Aubrun et al. (2019) conducted a round-robin test of actuator disks, comparing a mesh disk to a non-uniform disk with radially decreasing solidity. They showed that the disks are not overly comparable, and that the variation across facilities is quite large. Theunissen and Worboys (2018) examined the effect of hole topology on the produced drag and near-wake characteristics of actuator disks. With the exception of Aubrun et al. (2019) and Theunissen and Worboys (2018), few comparisons between the different disk design layouts have been conducted, and when actuator disks are used in experiments, the process of actuator disk selection is rarely explicit. The employed disk is simply said to have a certain design, and to match the two previously mentioned criteria of disk diameter and produced drag. Developing a standard actuator disk design which produces the desired wake would be both efficient and practical in order to create uniformity and comparability between experiments. In order to do so, however, more knowledge on the flow field behind actuator disks is needed.

After creating an actuator disk that matches the diameter and the produced drag, previous studies have examined the similarity of the flow field behind the actuator disk and the rotating model. The main question has been whether the wake can be properly modeled in the absence of the rotational momentum induced by rotating blades (Neunaber, 2018). Aubrun et al. (2013) used hot-wire measurements, and found that the wake of a rotating model and their porous disc in a modeled atmospheric boundary layer were indistinguishable at 3D downstream. A comparison at low turbulence inflow was also acceptable. Lignarolo et al. (2016b) conducted Particle Image Velocimetry (PIV) measurements on the wakes of both models. They showed that by matching the diameter and drag coefficient, the energy coefficient, velocity, pressure, enthalpy field and wake expansion matched, even in the absence of inflow turbulence. However, differences were found in terms of turbulence intensity and turbulent mixing within their field of view, stretching to 2.18D downstream, due to the presence of tip vortices behind the rotating model. They concluded that the wakes are in good agreement, and suggested the possibility to extend the use of the actuator disc model into the very near wake, given that turbulent mixing is correctly represented. Camp and Cal (2016) found that the mean kinetic energy transport in the far wake is adequately represented by the actuator disk, however in the near wake, significant discrepancies exist in the areas where rotation is a key phenomenon. Additionally, the main difference in the mean velocity in the near wake was the out-of-plane component, resulting from the rotation of the rotor, whereas the mean velocity is nearly the same in regions where rotation is not a critical phenomenon. They do, however, conclude that the results are encouraging for modelers who employ the actuator disk model for simulations of wind farms. Hence, there is a general agreement that the actuator disk is an adequate simplification in the far wake, and that there are certain discrepancies in the near wake, especially in the areas that are strongly affected by rotation when using a rotating model. However, the compared characteristics are usually mean flow characteristics. Despite a similarity of the mean flows, the instantaneous phenomena in the two wakes might still differ. Current literature examining the instantaneous flows and the fundamental structures constituting the flows is sparse. Camp and Cal (2019) compared a three-bladed rotating turbine model with an actuator disk using PIV. They applied snapshot Proper Orthogonal Decomposition (POD) and examined the invariants of the Reynolds stress anisotropy tensor, discovering discrepancies in the underlying spatial structures and the anisotropic character of the two wakes. While Camp and Cal (2019) have started to explore the issues of structural comparability of the wakes of actuator disks and rotating models, more research is needed to better understand the differences. By gaining more knowledge on how to improve the actuator disk model, it can become an accurate and simple tool for the industry.

The aim of this work is to examine how comparable a well matched actuator disk is to a rotating turbine instantaneously. The process of actuator disk selection is shown in detail, in order to determine how different disk designs and solidities affect the flow field. For all the studied flow characteristics, the full stream-wise 2D plane up to x/D = 3.3 is examined. This differs from the work of Aubrun et al. (2013) and Lignarolo et al. (2016b) who studied smaller fields of view, and Camp and Cal (2019) who conducted their POD analysis within limited sections of the downstream direction of their field of view. Further, the actuator disk whose wake mostly resembles the wake of the rotating model based on mean flow characteristics is chosen. The instantaneous phenomena and spatial structures in the wake of this actuator disk are examined and compared to the wake of the rotating model, in order to determine the potential similarities and differences of the underlying flow structures.

2. Experimental method

2.1. Facility

The experiments were conducted in a closed-loop wind tunnel that has a 1 m wide and 0.5 m tall test section. The inflow is uniform, with a maximum velocity of 35 m/s and a background turbulence intensity of 0.7%. It is the same facility as used by Skeide et al. (2020).

2.2. Test cases

Small-scale models were used in this study to examine the characteristics of models that are relevant for wind farm experiments, as mentioned in the introduction. The rotating wind turbine models used have two-bladed plastic rotors connected to a sliding bearing. The same models were used by Ebenhoch et al. (2017) and Segalini and Dahlberg (2020). Magnets are placed at the bottom of the tower to facilitate the mounting. They have a rotor diameter of $D = 45$ mm and a hub height of 65 mm.

The actuator disks were designed using SolidWorks and then 3D printed using an Ultimaker 2+ with PLA. Using computer-aided design and 3D printing implies that the disk designs can easily be shared and reproduced. The disks were designed with a diameter of 45 mm to match the rotating turbine, and a thickness of 2.5 mm. Two different actuator disks designs were tested. The first has uniform circular holes, comparable to those actuator disks that consist of a thin metal grid, as used by Aubrun et al. (2013) and Lignarolo et al. (2016b). Hereafter, the disks with this design will be referred to as Uniform Holes Disks (UHD). The second design has trapezoidal holes that increase in size as the radial coordinate increases, as used by Camp and Cal (2016, 2019). The solidity of these disks decreases with radial coordinate, matching a characteristic of an actual wind turbine. Disks with this design will be referred to as Nonuniform Holes Disks (NHD).

For each design, three different solidities were tested: 35%, 40% and 60%. The disks will be denoted UHD and NHD followed by the number describing their solidity, e.g. NHD35 for the 35% solidity disk with the NHD design. Due to limitations regarding printing thickness, providing low solidities with the UHD design proved problematic. Hence, the design was slightly changed in the disk with 35% solidity, allowing for the circular holes to also cover the edges of the disk. It was kept in mind that this resulted in a different disk circumference, meaning that this disk might not be directly comparable to the other UHDs. A solid disk was also made for reference. All the disks can be seen in figure 1.

The actuator disks were designed with a small hole in the center, in order to connect them to towers. This design resulted in a large solidity in the center of the disks, which can represent the nacelle of a wind turbine (Neunaber, 2018). The tower was designed to match the rotating model's tower, and a magnet was placed at the bottom of it.

2.3. Force measurements

Underneath the wind tunnel is a six-component AMTI BP40060HF 1000 force plate, able to measure the force and torque components along the x-, y- and z-axes. Here, x is defined to be in the downstream, longitudinal direction, y is upwards, and z completes a right-hand frame.

A test rig was constructed to measure the forces, consisting of a 0.5 m long magnetic steel bar that stretched along the width of the wind tunnel, on top of an aluminum cylinder that passed through a small hole in the floor of the tunnel. The cylinder was then attached to the force plate underneath the tunnel. The steel bar was lifted about 1 cm above the floor of the wind tunnel, to avoid any contact with the floor that could affect the force measurements, and to place the turbine in a uniform stream. A sketch of the setup, as well as the defined axes and origin, is shown in figure 2.

Three models were placed on the test rig while conducting the drag measurements. This was done to ensure that the drag would be within the load cell range so that slight changes in solidity would be noticeable. Using three models also averages out any small differences that might be present between the models. One model was placed in the center of the steel bar, at $z = 0$, and the other two were placed at a distance of 5D from it, i.e. at $z = \pm$ 5D.

The drag force in the x-direction was then measured for five different incoming wind velocities, corresponding to five different incoming Reynolds numbers $Re_D = \rho U_h D/\mu$, where ρ is the air density and μ is the air dynamic viscosity based on the measured temperature in the wind tunnel, and U_h is the incoming velocity at hub height. Drag measurements were also conducted having only the test rig and three towers inside the wind tunnel. Each measurement lasted 60 s with a sampling rate of 1000 Hz. Zero measurements were conducted before and after every measurement, to account for potential drift of the force plate. Measurement noise related to the transducer and the electrical equipment gave rise to some uncertainty. Nevertheless, the signal-to-noise ratio improved with the amplitude of the drag force. The lowest Reynolds number shown in the results was selected based on where the signal-to-noise ratio of the system became acceptable. For the Reynolds numbers presented, the uncertainty in the force measurements ranged from 0.9% to 4%.

2.4. Particle image velocimetry

For the PIV measurements, two LaVision Imager LX 16 megapixel cameras were used, combined with Sigma 180 mm 1:3.5D APO DG Macro lenses. The cameras were mounted outside of the wind tunnel, next to an acrylic window. The first and the second camera had their field of view just upstream and downstream of the turbine rotor, respectively, meaning that the two did not overlap. The first field of view had a range of $-3.01 \leq x/D \leq 0.01$ and $-1.12 \leq y/D \leq 0.92$, while the second had a range of $0.31 \leq x/D \leq 3.33$ and $-0.91 \leq y/D \leq 1.13$. Thus, the near-wake was captured by the second field of view, while the first field of view could be used to quantify the incoming velocity at hub height and to study the characteristics of the incoming flow. In some of the presented results, the data near the upper and lower edge of the field of view has been left out due to noise arising from particles entering and ex-

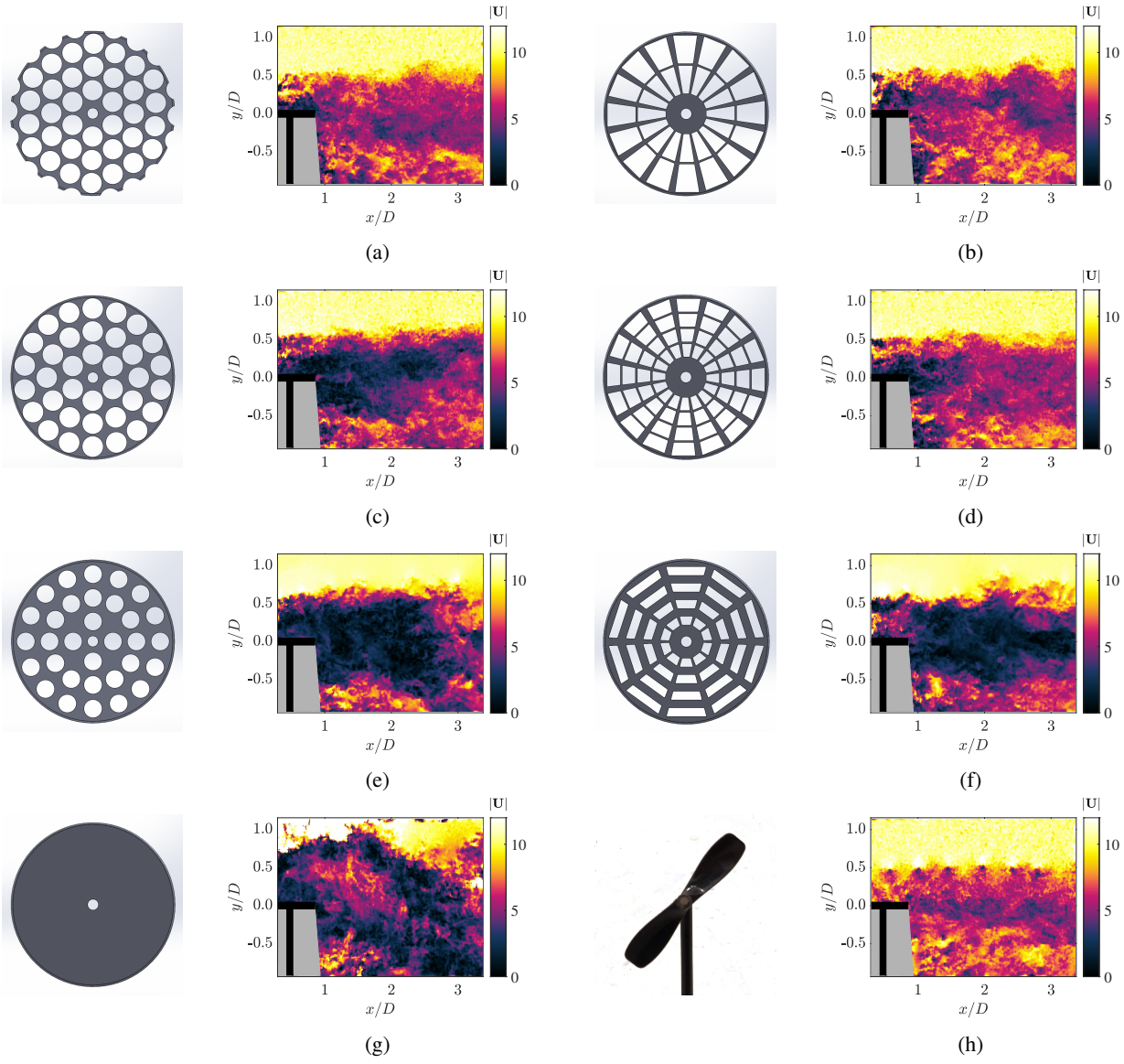

Figure 1: All actuator disk designs and a picture of the rotating model, next to an image of the instantaneous total velocity field behind the respective disk and the rotating model. (a) UHD35, (b) NHD35, (c) UHD40, (d) NHD40, (e) UHD60, (f) NHD60, (g) solid disk and (h) rotating model.

iting the domain.

A Litron Nano L200-15 laser, which is a Nd-YAG dual-pulse laser with a measured power of 208 mJ, was used to illuminate the particles. The laser sheet entered the wind tunnel through an acrylic window in the roof. The particles were seeded using a Magnum 2500 Hz smoke machine and the Martin Rush & Thrill Haze Fluid. A LaVision PTU X programmable timing unit was used to trigger and synchronize the laser and the cameras. In each measurement, 1000 frames were acquired by each camera. Further acquisition details are provided in table 1.

The recordings were acquired and processed using LaVision Davis 8.4. Background noise was subtracted from the images by subtracting the minimum value of every pixel over the entire data set, and then over a filter length of 29 images. Then, the local mean background intensity was filtered out by subtracting the sliding minimum over 20 pixels. The sliding average was calculated over five pixels using a Gaussian profile. Image correction was applied to correct for orthogonality. The processing was then performed with a window

Parameter	Value	Unit
Interframe time	50	μs
Acquisition rate	0.86	Hz
Number of samples	1000	
Field of view ($x \times y$)	3.02×2.04	D
Final window size	32×32	pixels
Window overlap	50	%
Vectors ($x \times y$)	307×207	

Table 1
PIV parameters used in data acquisition and processing.

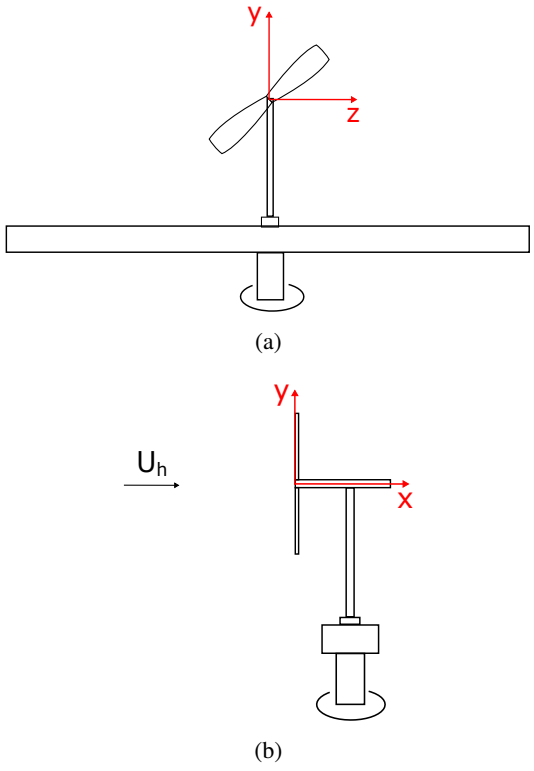

Figure 2: Sketch of one rotating turbine model on the test rig, with the defined axes, (a) from the point of view of the incoming flow and (b) from the side. The sketch is illustrative and not necessarily to scale.

size of 96×96 pixels and an overlap of 50% for the first pass, while the final window size was 32×32 pixels with an overlap of 50%. The resulting uncropped vector field consisted of 307 × 207 vectors.

2.5. Notation

The following notation is used when discussing the results. Each instantaneous velocity, corresponding to one location in one PIV frame, is denoted as $u = \overline{u} + u'$ and $v = \overline{v} + v'$ for the velocity in the $x-$ and $y-$directions, respectively, where u' and v' corresponds to the fluctuating parts of the velocity, and $\overline{u}$ and $\overline{v}$ is the mean velocity calculated by taking the mean over all 1000 statistically independent PIV measurements. The mean total velocity is $\overline{\mathbf{U}} = [\overline{u}, \overline{v}]$. The measurements are conducted in a 2D plane, and hence the out-of-plane velocity component $\overline{w}$ is not incorporated into the present analysis. Each characteristic calculated by taking the average over all the PIV measurements is denoted with an overbar.

3. Drag measurements

Since actuator disks are usually designed to match the drag of a rotating turbine, the first step was to conduct drag measurements. For each model and at each incoming Reynolds number, the average drag force over the 60 s measurement was calculated, and the drag resulting from the test rig and the towers was subtracted. As three models were used during the drag measurements, the drag force was then divided by three, arriving at the drag acting on only one disk or one set of rotating blades. The drag coefficient was calculated as

$$C_D = \frac{F_D}{\frac{1}{2}\rho U_h^2 A}, \tag{1}$$

where $A = \pi D^2/4$ is the reference area of the turbine or the actuator disk. The drag coefficient as a function of Reynolds number is plotted in figure 3 for all the models.

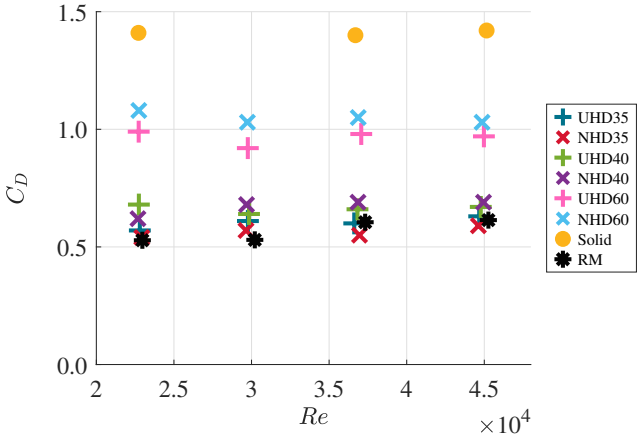

Figure 3: The drag coefficient as a function of incoming Reynolds number for all turbine models.

Lignarolo et al. (2016b) showed drag coefficients as a function of actuator disk solidity based on the results presented in six different papers, and concluded that the drag coefficient decreases approximately linearly with decreasing solidity. That is also the case for the current measurements. As expected, the solid disk produces a much higher drag coefficient than the rotating model. The drag coefficient of the solid disk at $Re_D = 3 \times 10^4$ is omitted from the figure, as it deviates from the others by more than 42 standard deviations, and is thus regarded as an outlier.

The drag coefficients seem to concentrate around some mean value, suggesting that the non-dimensional drag is Reynolds number independent over this range. The average drag coefficient over the different Reynolds numbers was calculated, along with the standard deviation, and is presented in table 2 for the rotating model and the actuator disks with 35% and 40% solidity. The NHD35 is the best match compared to the drag coefficient of the rotating model, with a deviation of 1.8%. It is closely followed by the UHD35, which has a deviation of 5.3%.

4. Reynolds number dependence of the velocity field

For the rotating model and both actuator disks with 35% solidity, PIV measurements were conducted at five different incoming Reynolds numbers, relating to five different incoming flow velocities at hub height, U_h. This was done to check whether the normalized velocity in the wake would

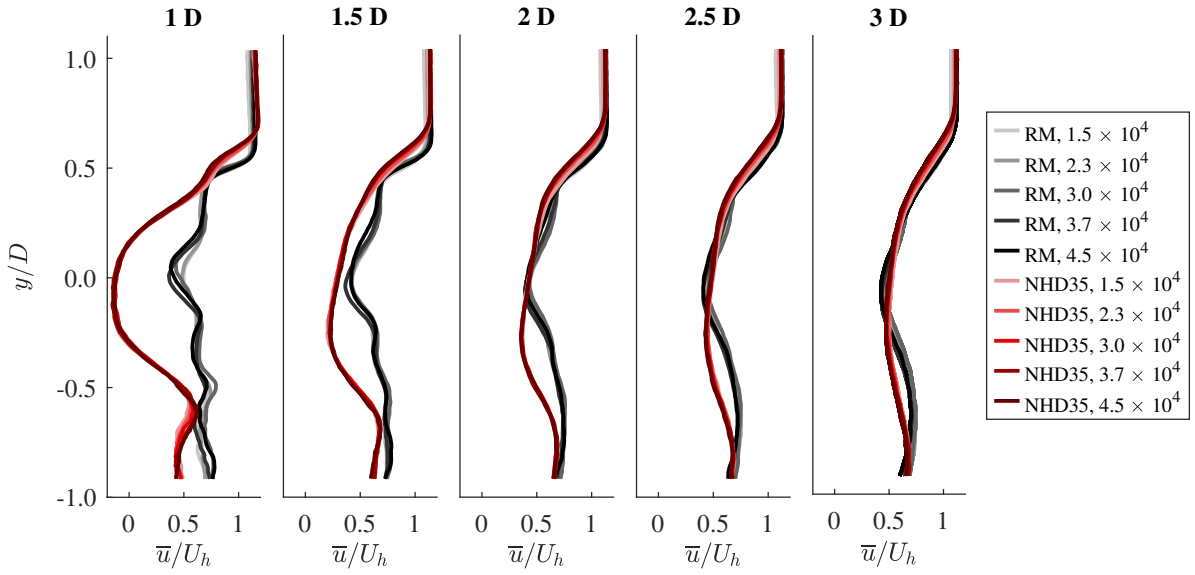

Figure 4: Normalized $\overline{u}$ velocity downstream of the rotating turbine model, RM, and the NHD35 actuator disk for different incoming Reynolds numbers.

Disk type	Average C_D	C_D standard deviation
RM	0.57	0.08
UHD35	0.60	0.05
NHD35	0.56	0.05
UHD40	0.66	0.05
NHD40	0.67	0.06

Table 2
Average C_D for the rotating model and the disks with 35% and 40% solidity across measurements taken at different Reynolds numbers, and the associated standard deviation.

vary as a function of the incoming Reynolds number, since the non-dimensional drag was Reynolds number independent in this regime. The mean velocity field was calculated and then normalized by U_h. The stream-wise velocity component is the dominant component of the total velocity. Hence, figure 4 depicts the stream-wise velocity component at five downstream locations for all five incoming Reynolds numbers, for the rotating model and the NHD35. The first cross-section is placed shortly behind the end of the model tower, and the last cross-section is placed close to the end of the field of view.

For the actuator disk, the normalized velocity profiles overlap at all the downstream locations. On average, the standard deviation between the measurements as a percentage of the mean value is 2.4% in the entire field of view. The same analysis was conducted on the UHD35, showing equally good agreement, with the velocity profiles similarly collapsed. Thus, the actuator disks are independent of Reynolds number within the investigated range.

For the rotating model, the lines illustrating the normalized stream-wise velocity generally follow the same pattern and largely overlap already at 1D downstream. By 3D downstream, the velocity profiles are in very good agreement. However, it can be seen that the two lowest Reynolds numbers produce a slightly different profile 1D downstream, e.g. behind the nacelle at $y/D = 0$, implying that the rotating model's wake is only Reynolds number independent above some threshold Reynolds number. Studying the three highest Reynolds numbers, starting at $Re_D = 3\times10^4$, an average standard deviation of 3.3% of the mean value is found.

Based on these results, combined with the drag measurements, $Re_D = 1.5 \times 10^4$ and $Re_D = 2.3 \times 10^4$ are outside the Reynolds number independent regime. Accordingly, the rest of the PIV measurements were performed at the lowest Reynolds number within the Reynolds independent regime, $Re_D = 3 \times 10^4$, in order to limit other detrimental factors, e.g., the models auto-yawing inadvertently during a test.

5. Mean velocity fields

The velocity in the wake is the first characteristic used to compare the rotating model with the actuator disks. The time average total velocity $|\overline{\mathbf{U}}|$ was normalized by using the incoming velocity U_h, and is depicted in figure 19 for the rotating model and each actuator disk. The vectors indicate the magnitude and the direction. A mask has been applied over the model and to the area affected by shadows and laser reflection near the tower. The total velocity up to 1D upstream of the models is also included in figure 19.

The total velocity upstream of the actuator disks indicates that the incoming flow slows down directly in front of the disks, and that the slowdown increases in magnitude and covers a larger area as the solidity of the disks increase. The slowdown in front of the blades of the rotating model has a smaller magnitude than what can be seen for the 35% solidity disks, showing that the rotating model imposes less of a blockage to the incoming flow. Although subtle, this result has implications for blockage estimates made for wind farms using either free rotating models or actuator disks, which

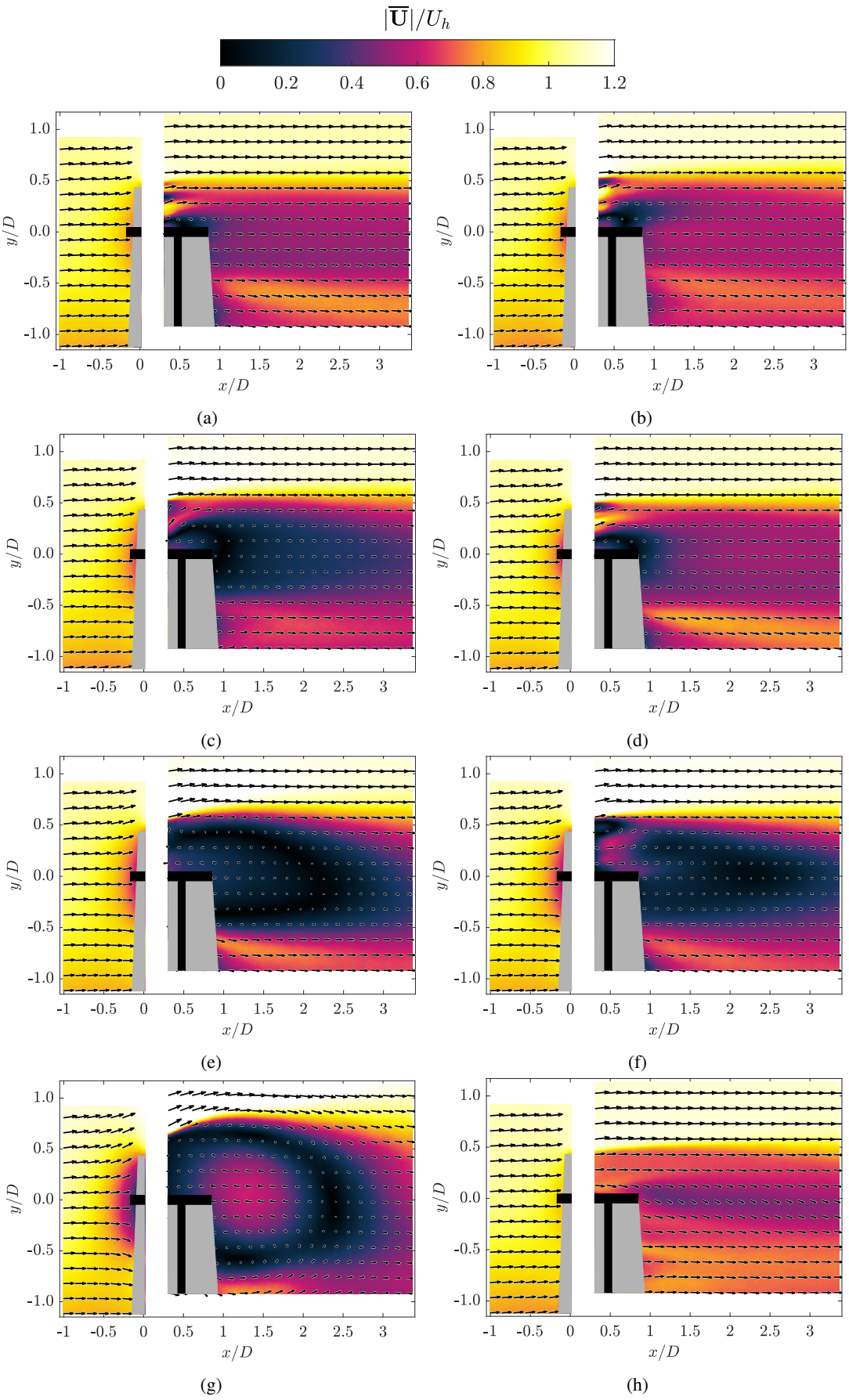

Figure 5: Normalized total velocity fields for (a) UHD35, (b) NHD35, (c) UHD40, (d) NHD40, (e) UHD60, (f) NHD60, (g) solid disk and (h) rotating model.

have been illustrated to have different blockage effects here.

When studying the wakes, a first observation is that the UHD design seems to produce a larger velocity deficit compared to the NHD design. Furthermore, the solid actuator disk can be seen to produce a large recirculation area, due to the large blockage produced by the bluff body. The UHD60 also induces a large area of reversed flow, and neither are thus comparable to the rotating model. The remaining actuator disks have a small recirculation area directly behind the disk, that is only present less than 1D downstream, and thus only affects the comparability of the disks and the rotating model in the immediate wake.

It is evident that the solid disk and the disks with 60% solidity have considerable areas of deviation from the rotating model, which agrees with the drag measurements. Furthermore, the 40% solidity disks deviate more from the rotating model than the 35% disks, which again agrees with the drag measurements. UHD35 and NHD35 both show good agreement with the rotating model, with the main difference being prior to 1D downstream. The two have similar magnitude of deviation after 1D, however the UHD35 is slightly closer to the rotating model when averaging the absolute value of the deviations.

Figure 6 shows the normalized $\overline{u}$ velocity, being the dominant velocity component, at five different downstream locations as well as one upstream location. The tip vortices present at the upper edge of the rotating model's wake (distinctly visible in figure 1h and comparable to those found by Hong et al. (2014)) induce a steep velocity gradient seen at 1D downstream. The gradient then flattens as one moves farther downstream and the tip vortices lose strength. The actuator disks show a smoother transition between the freestream and the wake at 1D downstream. The velocity variations in the wake of the actuator disks homogenize quickly compared to the rotating model's wake. This is because the actuator disks transfer kinetic energy in the flow into turbulence which quite quickly decays (Batchelor and Townsend, 1947, 1948a,b). Overall, figure 6 indicates that the magnitude of the $\overline{u}$ velocity behind the rotating model coincides with the magnitude of the $\overline{u}$ velocity created by both 35% solidity disks and NHD40 from 1.5D downstream.

6. Vorticity

In order to understand the organization of vortical structures in the wake of the rotating model and the actuator disks, the vorticity is examined. The time average out-of-plane vorticity $\overline{\omega_z}$ was normalized using the incoming flow velocity U_h and the disk diameter D. Figure 7 shows the normalized vorticity for each actuator disk and the rotating model. The solid disk and the disks with 60% solidity create two distinct areas of high magnitude vorticity, covering large parts of the wake, and thus differ from the lower solidity disks which seem to mainly produce vorticity at the upper and lower edges of the wake. This vorticity seen at the edges of the wake may be caused by vortices created at the disk edges or as a result of the interaction between the wake and the free-stream. Additional vorticity is present directly behind the actuator disks, which is likely caused by the turbulent flow through the holes in the disks, and the interaction of these flows behind the disks (Ertunç et al., 2010; Mazellier and Vassilicos, 2010).

The rotating model also produces high levels of vorticity along the upper and lower edges of the wake, as a result of tip vortices from the rotor blades. The upper line of vorticity is stronger and preserves its strength for a longer distance downstream than is the case with the low solidity actuator disks. However, towards the end of the field of view, this strong vortex sheet breaks down and the vorticity diffuses. There is also vorticity present in the center of the wake of the rotating model, possibly representing the root vortex from the hub (Lignarolo et al., 2016b).

Once again, the 40% and 35% solidity disks resemble the rotating turbine the most. In the case of these lower solidity disks, the main difference is seen prior to 1D downstream. Downstream of 1D, both 35% solidity disks have the same magnitude of deviation from the rotating model, with NHD35 being the closest match downstream of 1.5D.

Going forth, the analysis will be focused on only one actuator disk. In this case, the wakes of both 35% solidity disks replicate the wake of the rotating model well. Since NHD35 is a slightly closer match in terms of the drag and the mean vorticity field, the remaining analysis will focus on NHD35. The chosen disk is compared to the rotating model for several mean metrics, in a similar manner to previous actuator disk studies. However, in this case, in order to gain knowledge about the underlying mechanisms of the flow, more than just mean quantities are studied.

The mean vorticity field is a result of instantaneous swirl, and thus, the instantaneous swirl can provide information about the flow structures that cause vorticity in the flow. Swirling strength is defined as the second invariant of the velocity gradient tensor as described by Jeong and Hussain (1995). Figure 8 shows an image of the instantaneous swirling strength, signed by vorticity, for the rotating model and the NHD35. These images are representative of the 1000 PIV measurements that were taken. The main difference between the two is the strong, distinct swirl seen at the upper edge of the wake for the rotating model, caused by tip vortices from the rotor blades. The actuator disk also has some swirl in the upper part of the wake, however it has a significantly lower strength than the distinct vortices from the rotating model, and it resembles the swirl at the lower edge of the wake and close to the wind tunnel floor. This swirl may be formed by the roll-up of the shear layer produced by the presence of the disk. The actuator disk also has high intensity swirl directly behind the disk, not seen after the rotating model's blades. As previously mentioned, this swirl is believed to be caused by the turbulent flow passing through the holes in the disk and the interaction of the jets behind the disk.

The important finding here is that even though averaging of the measurements resulted in similar sheets of vorticity at the upper edge of the wake, with an average local differ-

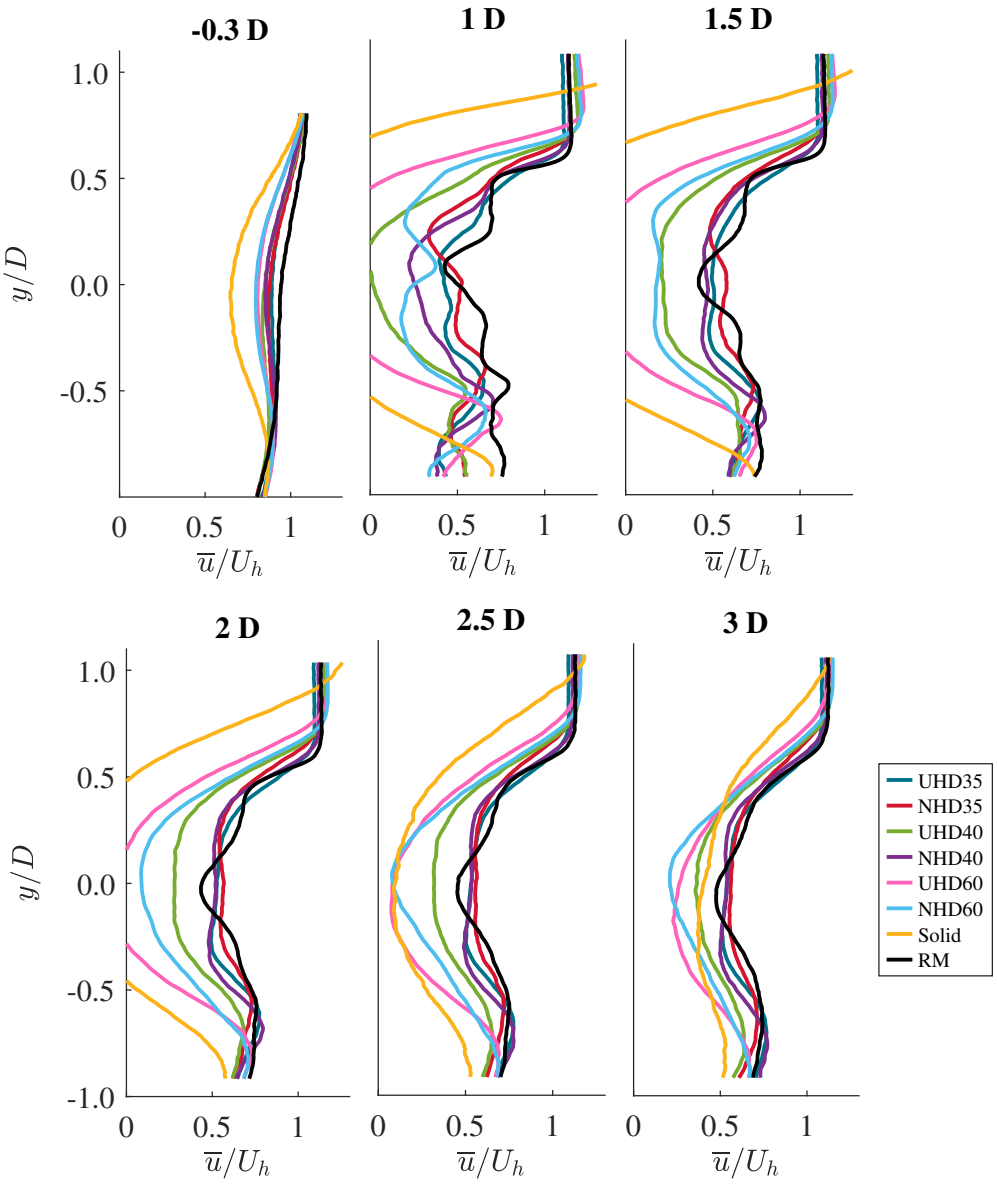

Figure 6: Normalized $\overline{u}$ velocity at one upstream and five downstream locations for the rotating turbine model and each actuator disk.

ence of less than 5% in the last half of the field of view, the instantaneous vortex structures differ. Many previous studies have used porous style disks which approximately match the drag and mean fields (Lignarolo et al., 2016b; Camp and Cal, 2016; Bossuyt et al., 2017). However, as indicated here when studying the instantaneous fields, the phenomenology in the flows might still be different.

7. Reynolds stresses

Another mean flow characteristic often examined when comparing actuator disks and rotating models is the normal and shear Reynolds stresses. The normal Reynolds stresses are investigated through the time average turbulence intensity, expressed as the normalized root of the mean 2D turbulent kinetic energy

$$\frac{\sqrt{k_{2D}}}{U_h} = \frac{\sqrt{\frac{1}{2}(\overline{u'u'} + \overline{v'v'})}}{U_h}, \tag{2}$$

where $\overline{u'u'}$ and $\overline{v'v'}$ are the mean normal Reynolds stresses in the stream-wise and wall-normal direction, respectively. The time average turbulence intensity in the wake of the rotating model and the NHD35 can be seen in figure 9.

The rotating model shows high turbulence intensity at the upper edge of the wake, stemming from the tip vortices. Towards the end of the field of view, the tip vortices start to break down, and the turbulence diffuses. The turbulence intensity at the upper edge of the wake behind the actuator disk indicates that vortices emerging at the disk edge are present in close vicinity of the disk, for $x/D < 1$. However, this tur-

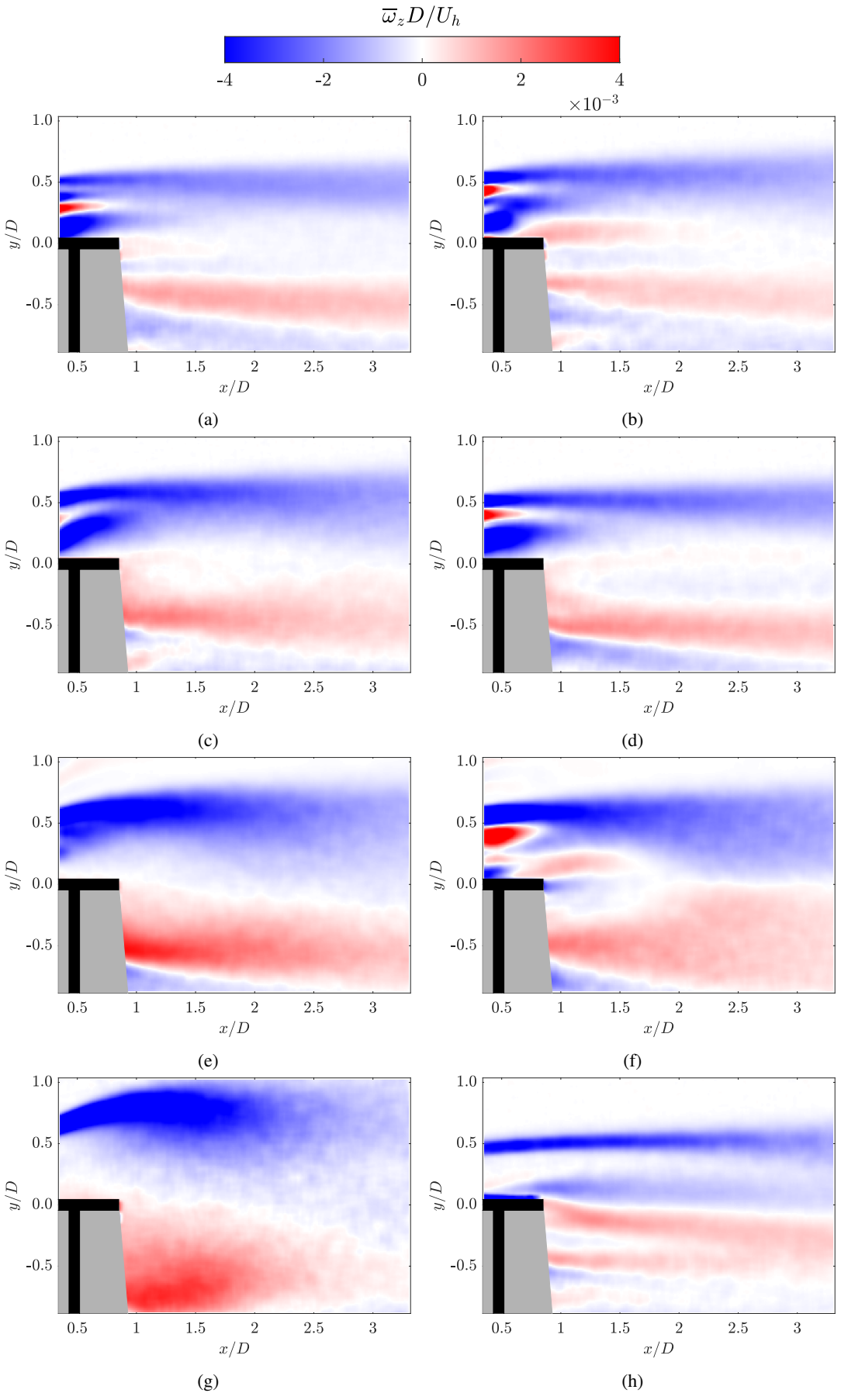

Figure 7: Normalized vorticity fields for (a) UHD35, (b) NHD35, (c) UHD40, (d) NHD40, (e) UHD60, (f) NHD60 and (g) solid disk and (h) rotating model.

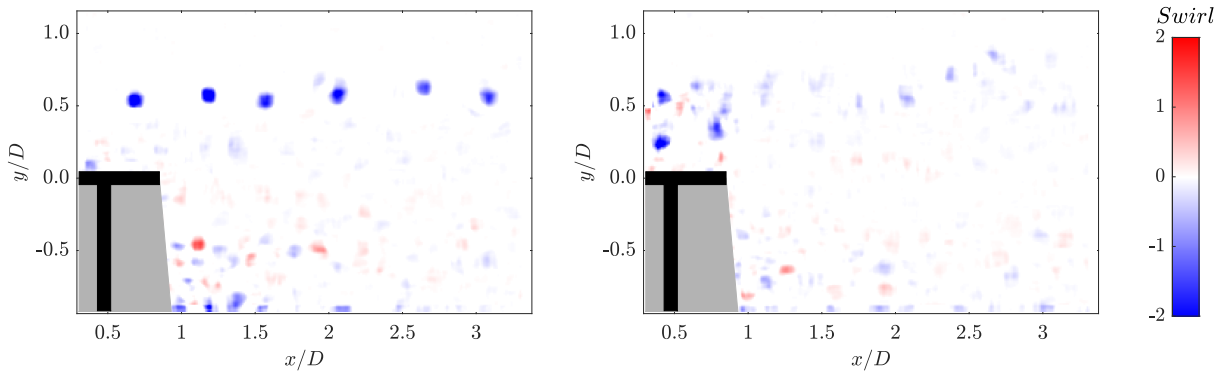

Figure 8: Instantaneous swirling strength signed by vorticity, for (a) the rotating model and (b) NHD35.

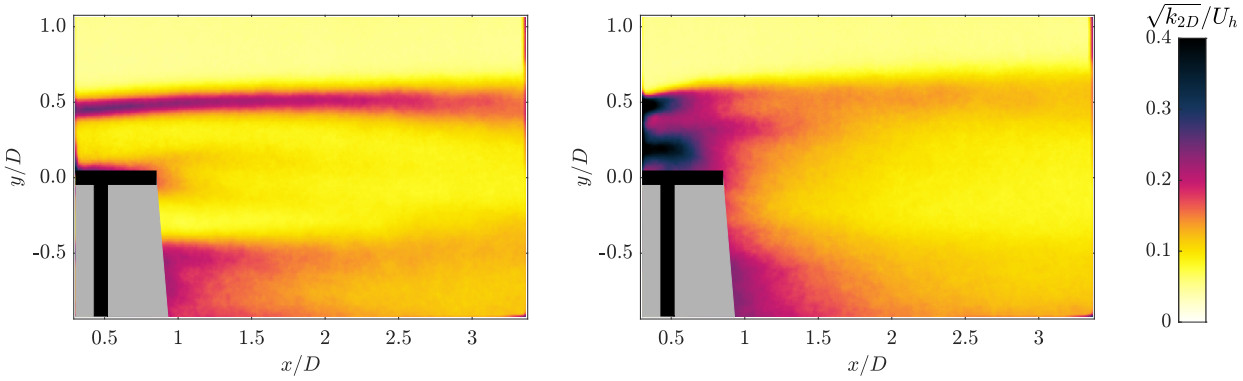

Figure 9: Turbulence intensity fields for (a) the rotating model and (b) NHD35.

bulent structure quickly diffuses. The actuator disk shows a high concentration of turbulence intensity directly behind the disk, which then slowly diffuses throughout the wake. This highly turbulent region is likely caused by the turbulent mixing of the jets and the small recirculation zone as observed in section 5, akin to grid turbulence (Ertunç et al., 2010). The most evident difference between the two wakes is in this region shortly behind the disk, less than 1D downstream. Downstream of 2D, the average difference between the two fields is 12%.

The mean in-plane Reynolds shear stress, $\overline{u'v'}$, normalized with the incoming velocity squared, is shown in figure 10a for the rotating model and 10b for NHD35. The shear stress $\overline{u'v'}$ physically represents the vertical flux of momentum, with negative values indicating downward flux and positive values indicating upward flux. Hence it can be seen that for both models, the upper part of the wake is dominated by negative $\overline{u'v'}$ and the lower part is dominated by positive $\overline{u'v'}$.

Both the rotating model and NHD35 produce more intense shear stress in the shear layer of the wake, caused by flow entrainment and mixing. For the actuator disk, an increased intensity of shear stress is observed directly after the disk, likely caused by the same phenomena that causes increased normal stresses in this area, i.e., the turbulent mixing of the flow passing through the holes in the disk. The largest difference between the two flow fields is found in this region, for $x/D < 1$. Figure 11 illustrates the shear stress along three downstream cross-sections. As can be seen, the differences between the shear stress produced by the two models diminishes as one moves farther downstream, and the shear stress is largely of the same order of magnitude. Thus, the mean characteristic of Reynolds stresses is comparable between the static and the rotating model.

8. Proper orthogonal decomposition

As the swirl indicated that the instantaneous phenomena in the wakes differ between the rotating model and NHD35, it was decided to look at the spatial modes that make up the wake, to gain an understanding of the underlying spatial structures in the flows. In order to examine this, POD was applied. POD was first developed in fluid mechanics by Lumley (1967). Sirovich (1987) then developed the method of snapshot POD, where each instantaneous PIV measurement is considered to be a snapshot of the flow. The analysis conducted in this study followed the steps described by Meyer et al. (2007).

Snapshot POD is used to find the spatial modes of the

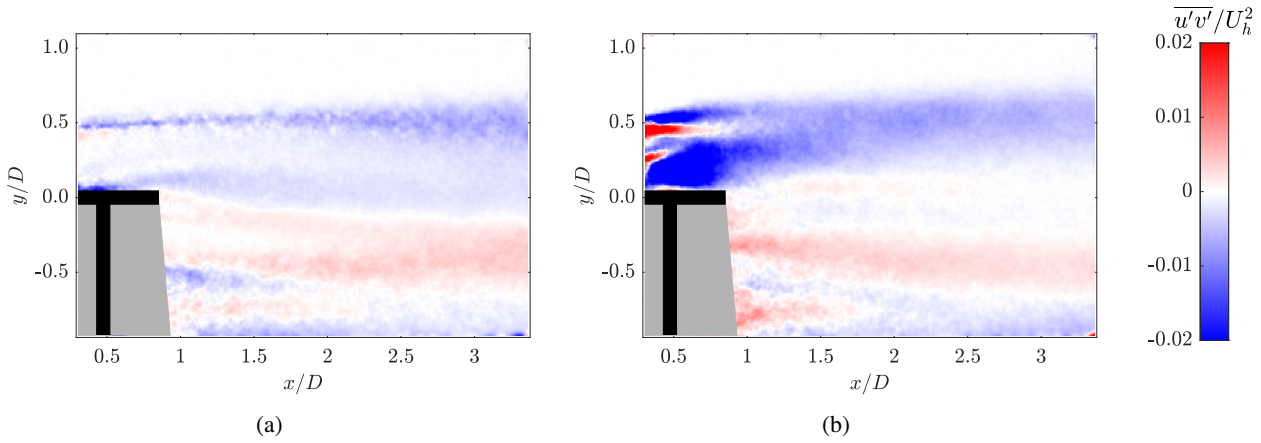

Figure 10: Normalized Reynolds shear stress fields for (a) the rotating model and (b) NHD35.

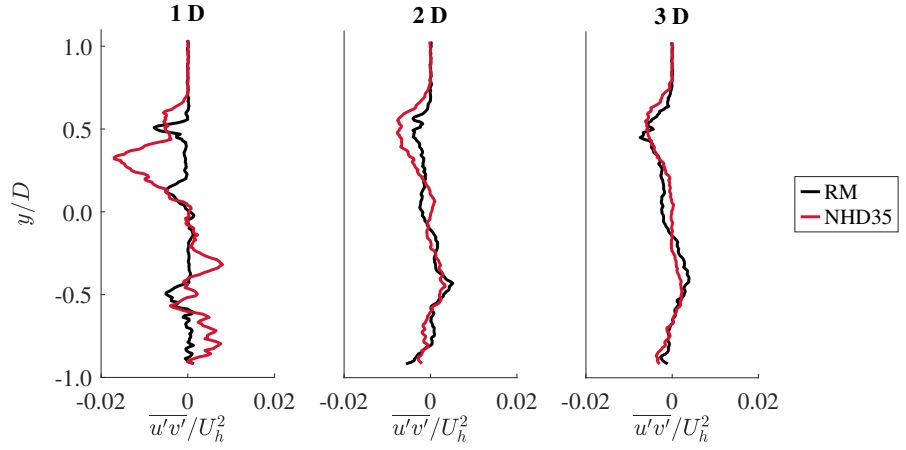

Figure 11: Normalized Reynolds shear stress $\overline{u'v'}$ at three locations downstream of the rotating model and the NHD35.

flow. The mean velocity field is considered to be the zeroth mode. The analysis then focuses on the fluctuating parts of the velocity components. The method states that each snapshot can be expanded in a series of POD modes. Thus, if $\mathbf{u}'^n$ is a vector containing all the fluctuating u' and v' velocities in snapshot n, $[u_1'^n ... u_M'^n v_1'^n ... v_M'^n]^T$, where M is the number of positions in the snapshot,

$$\mathbf{u}'^n = \sum_{i=1}^{N} a_i^n \boldsymbol{\phi}^i. \tag{3}$$

Here, $\boldsymbol{\phi}^i$ are the POD modes, and a_i^n are the POD coefficients related to snapshot n, determined by projecting the fluctuating part of the velocity field onto the POD modes. The analysis was performed on $N = 1000$ snapshots for each model.

The modes are ordered by their energy content, with lower numbered modes having higher energy content than higher numbered modes. Figure 12 displays the cumulative energy of the modes for the rotating turbine model and all the actuator disks. The NHD35 is the actuator disk which most closely resembles the rotating model in terms of the magnitude of energy contained in each mode. Additionally, both the rotating model and the NHD35 seem to have two especially energetic modes.

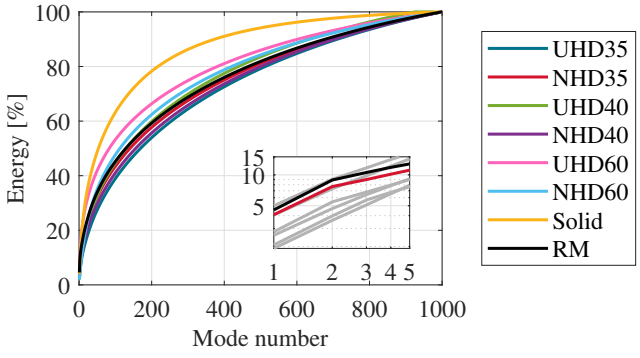

Figure 12: Cumulative energy of the modes for all actuator disks and the rotating model. The inset is zoomed in on the five most energetic modes, with RM and NHD35 highlighted, showed in log-log space.

Since 1000 vector fields have been used in making the modes, 1000 modes would be required to capture all the energy in the velocity fluctuations. The number of modes required to capture a certain fraction of the energy can however provide some indication on the number of modes required to make a relevant approximation of the fluctuating

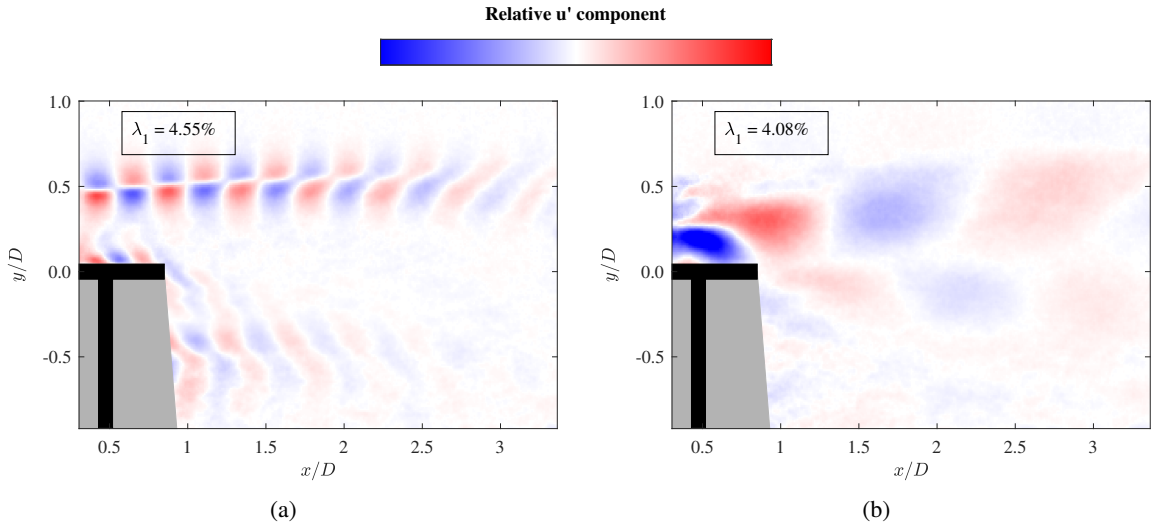

Figure 13: The first u' velocity mode for (a) the rotating model and (b) NHD35. Only the relative values are of importance.

velocity (van der Kindere and Ganapathisubramani, 2018). It can be worth noting at this point that all the models require a relatively large number of modes to capture 50 % of the energy in the flow, the rotating model requiring 129 modes and the NHD35 requiring 140 modes. This suggest that even though the few most energetic modes might provide information about the most energetic structures in each flow, the flows are not constructed of a few large, energetic structures. Rather, they seem to be complex flows with large amounts of local fluctuations, requiring many modes to be described. It should also be noted that certain portions of the total energy might result from measurement noise and other PIV related issues, as discussed by van der Kindere and Ganapathisubramani (2018).

When high-energy modes are present, these usually represent periodic, large-scale flow structures. However, the amount of energy contained in the modes does not imply anything about the shapes of the modes. Figure 13 and 14 show the first mode of the fluctuating velocity components u' and v', respectively, for the rotating turbine and the NHD35. When examining the modes, the absolute values are insignificant, as each mode is coupled with a relative POD coefficient when used to reconstruct the fluctuating velocities in a snapshot. The important factor is the relative values, demonstrating the length scale and location of the velocity fluctuations that contain a certain fraction of the total energy.

The first mode of the rotating turbine shows high intensity turbulent kinetic energy at the upper and lower edges of the wake, which seem to represent the kinetic energy in the tip vortices from the blades. These energetic structures start right behind the rotor blades and are still visible at the end of the field of view, but do however seem to decrease in intensity farther downstream. As previously mentioned, Camp and Cal (2019) studied the POD modes of actuator disks and rotating models in the xy plane. They found a prominent feature near the top tip of the wake in the first u' velocity mode. However, the tip vortices found behind the rotating model in figure 13 are more distinct. Additionally, tip vortices can be observed in the v' velocity mode in this case. To the authors knowledge, this is the first explicit demonstration of such distinct tip vortices in the stream-wise xy plane emerging from the POD modes.

The first mode stemming from the NHD35 also demonstrates repeating structures in the wake, suggesting a periodic shedding structure is also present for this disk, but with very different dynamics to that in the wake of the rotating model. There is high intensity turbulent kinetic energy directly behind the disk, suggesting high velocity fluctuations at this location. These fluctuations might be connected to the turbulent mixing of the flow jets passing through the holes in the disk.

Comparing the modes of the rotating model and the NHD35, it is evident that the most energetic structures in the two flows are fundamentally different. The energetic structures in the modes of the rotating model are concentrated around the edges of the wake, whereas for NHD35, the energetic structures are to a larger extent present in the center of the wake. A difference can also be seen in terms of the length scale of the structures. The rotating model indicates small energetic structures, with the velocity fluctuations quickly changing direction. The actuator disk illustrates significantly larger, and thus fewer, structures. As previously seen in terms of the instantaneous swirling strength, the tip vortices stemming from the rotating model are evident, and such strong tip vortices does not appear in the case of the actuator disk. None of the actuator disks showed similar behavior as the rotating model when studying their modes. Hence, together with the work of Camp and Cal (2019), the underlying differences in the wakes of rotating models and actuator disks are here indicated.

9. Conclusion

The near wake of a lab-scale rotating wind turbine model and multiple actuator disks of the same dimensions were

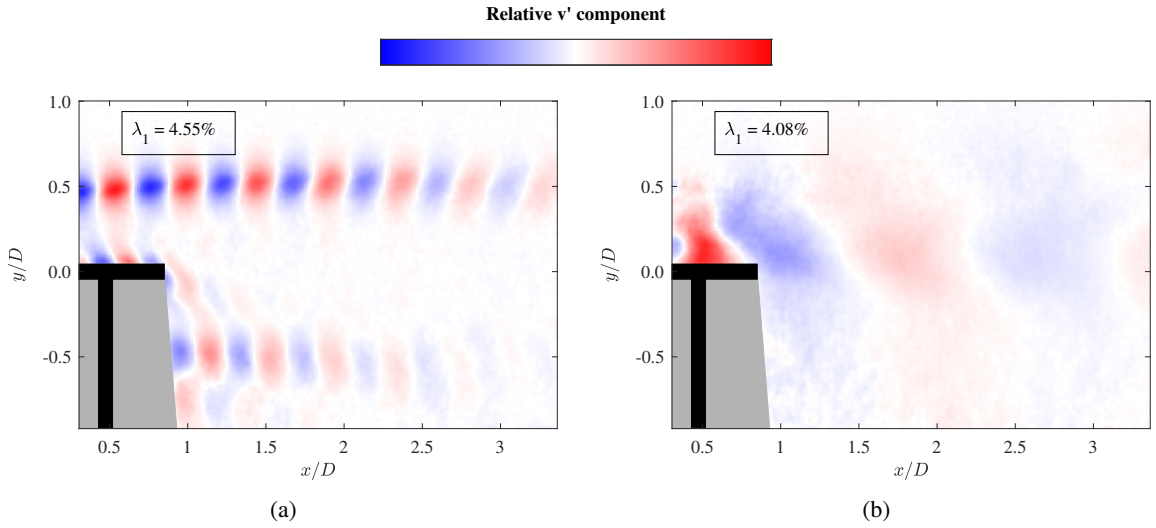

Figure 14: The first v' velocity mode for (a) the rotating model and (b) NHD35. Only the relative values are of importance.

studied experimentally in a wind tunnel with PIV. Actuator disks of two different designs and multiple different solidities were used. The process of actuator disk selection, which is often implicit in actuator disk research, is explicitly shown by presenting the results from drag measurements as well as the mean velocity and vorticity fields in the wake resulting from the PIV.

The normalized total velocity in the wake of the rotating model and each actuator disk was compared, showing that the high solidity disks had too large blockage, which led to a significant velocity decrease in the wake. The velocity field emerging behind the low solidity disks coincided well with the wake of the rotating model. All actuator disks showed a recirculation region, however limited to $x/D < 1$ for the 35% solidity disks.

The out-of-plane vorticity in the wakes was then compared. The rotating model showed increased intensity of vorticity along the upper edge of the wake, induced by tip vortices. The actuator disks also showed increased levels of vorticity along the edges of the wake. The lower solidity disks showed high intensity vorticity directly behind the disks, induced by turbulent mixing of the flow jets passing through the holes of the disks.

Overall, both disks with 35% solidity closely replicated the wake of the rotating turbine, however the NHD35 was a slightly closer match and was thus studied in further detail. Since the mean vorticity field is a result of instantaneous swirl, the instantaneous swirling strength signed by vorticity was studied. It demonstrated that instantaneous tip vortices were present behind the rotating model, but not behind the NHD35. Additionally, high intensity swirl was seen directly behind the actuator disk, again assigned to the mixing of the flow jets through the disk holes.

The mean normal and shear Reynolds stresses of the NHD35 and the rotating model were comparable. The difference between the two wakes was limited to the area $x/D < 1$.

POD analysis was conducted to analyze the underlying phenomena of the two flows. It showed how the most energetic mode for the rotating model represented the upper and lower tip vortices, which were not present for the actuator disk. The energetic velocity fluctuations differed both in terms of length scale and location. This implies that the main structures constituting the two flows are different.

Despite having fairly good agreement between the rotating model and the actuator disk across many mean parameters, including drag, velocity, vorticity and shear stress, the modal structure of the flows are still different. The underlying, instantaneous flow phenomena in the near wake of the actuator disk are thus not representative of a rotating model.

Actuator disks are clearly good for capturing mean flow properties, but as this study has shown, instantaneous phenomena in the wake are not always well captured. Moreover, the upstream blockage effect of the actuator disks and rotating turbines differed. Therefore, as actuator disks will continue to be used, it is important to understand all aspects of their flow behavior. This will contribute to a better understanding in studies in which they are employed, and may also help in the development of different disk designs which better capture higher order and instantaneous flow features.

References

Aubrun, S., Bastankhah, M., Cal, R., Conan, B., Hearst, R., Hoek, D., Hölling, M., Huang, M., Hur, C., Karlsen, B., Neunaber, I., Obligado, M., Peinke, J., Percin, M., Saetran, L., Schito, P., Schliffke, B., Sims-Williams, D., Uzol, O., Vinnes, M., Zasso, A., 2019. Round-robin tests of porous disc models. Journal of Physics: Conference Series 1256, 012004. URL: https://doi.org/10.1088%2F1742-6596%2F1256%2F1%2F012004, doi:10.1088/1742-6596/1256/1/012004.

Aubrun, S., Loyer, S., Hancock, P., Hayden, P., 2013. Wind turbine wake properties: Comparison between a non-rotating simplified wind turbine model and a rotating model. Journal of Wind Engineering and Industrial Aerodynamics 120, 1–8. doi:10.1016/j.jweia.2013.06.007.

Barthelmie, R., Churchfield, M., Moriarty, P., Lundquist, J., Oxley, G., Hahn, S., Pryor, S., 2015. The role of atmospheric stability/turbulence

on wakes at the egmond aan zee offshore wind farm. Journal of Physics: Conference Series 625. doi:10.1088/1742-6596/625/1/012002.

Barthelmie, R.J., Jensen, L.E., 2010. Evaluation of wind farm efficiency and wind turbine wakes at the Nysted offshore wind farm. Wind Energy 13. doi:10.1002/we.408.

Batchelor, G., Townsend, A., 1947. Decay of vorticity in isotropic turbulence. Proceedings of The Royal Society A: Mathematical, Physical and Engineering Sciences 190, 534–550. doi:10.1098/rspa.1947.0095.

Batchelor, G.K., Townsend, A.A., 1948a. Decay of isotropic turbulence in the initial period. Proceedings of the Royal Society of London. Series A, Mathematical and Physical Sciences 193, 539–558. URL: http://www.jstor.org/stable/98061.

Batchelor, G.K., Townsend, A.A., 1948b. Decay of turbulence in the final period. Proceedings of the Royal Society of London. Series A, Mathematical and Physical Sciences 194, 527–543. URL: http://www.jstor.org/stable/98265.

Blackmore, T., Batten, W., Muller, G., Bahaj, A., 2013. Influence of turbulence on the drag of solid discs and turbine simulators in a water current. Experiments in Fluids 55. doi:10.1007/s00348-013-1637-9.

Bleeg, J., Purcell, M., Ruisi, R., Traiger, E., 2018. Wind farm blockage and the consequences of neglecting its impact on energy production. Energies 11. doi:10.3390/en11061609.

Bossuyt, J., Howland, M., Meneveau, C., Meyers, J., 2017. Measurement of unsteady loading and power output variability in a micro wind farm model in a wind tunnel. Experiments in Fluids 58. doi:10.1007/s00348-016-2278-6.

Branlard, E., 2017. Velocity Field Upstream of Aligned and Yawed Rotors: Wind Turbine and Wind Farm Induction Zone. pp. 321–332. doi:10.1007/978-3-319-55164-7_24.

Camp, E., Cal, R., 2016. Mean kinetic energy transport and event classification in a model wind turbine array versus an array of porous disks: Energy budget and octant analysis. Physical Review Fluids 1, 044404. doi:10.1103/PhysRevFluids.1.044404.

Camp, E., Cal, R., 2019. Low-dimensional representations and anisotropy of model rotor versus porous disk wind turbine arrays. Physical Review Fluids 4. doi:10.1103/PhysRevFluids.4.024610.

Ebenhoch, R., Muro, B., Dahlberg, J.Å., Berkesten Hägglund, P., Segalini, A., 2017. A linearized numerical model of wind-farm flows. Wind Energy 20, 859–875. URL: https://onlinelibrary.wiley.com/doi/abs/10.1002/we.2067, doi:10.1002/we.2067.

Ertunç, O., Ozyilmaz, N., Lienhart, H., Durst, F., 2010. Homogeneity of turbulence generated by static-grid structures. Journal of Fluid Mechanics 654, 473–500. doi:10.1017/S0022112010000479.

Forsting, A.R.M., Bechmann, A., Troldborg, N., 2016. A numerical study on the flow upstream of a wind turbine in complex terrain. Journal of Physics: Conference Series 753. URL: https://doi.org/10.1088%2F1742-6596%2F753%2F3%2F032041, doi:10.1088/1742-6596/753/3/032041.

Forsting, A.R.M., Troldborg, N., 2015. The effect of blockage on power production for laterally aligned wind turbines. Journal of Physics: Conference Series 625. URL: https://doi.org/10.1088%2F1742-6596%2F625%2F1%2F012029, doi:10.1088/1742-6596/625/1/012029.

Harrison, M., Batten, W., Myers, L., Bahaj, A., 2010. Comparison between CFD simulations and experiments for predicting the far wake of horizontal axis tidal turbines. Renewable Power Generation, IET 4, 613 – 627. doi:10.1049/iet-rpg.2009.0193.

Hong, J., Toloui, M., Chamorro, L., Guala, M., Howard, K., Riley, S., Tucker, J., Sotiropoulos, F., 2014. Natural snowfall reveals large-scale flow structures in the wake of a 2.5-MW wind turbine. Nature communications 5, 4216. doi:10.1038/ncomms5216.

Howland, M.F., Bossuyt, J., Martínez-Tossas, L.A., Meyers, J., Meneveau, C., 2016. Wake structure in actuator disk models of wind turbines in yaw under uniform inflow conditions. Journal of Renewable and Sustainable Energy 8. URL: https://doi.org/10.1063/1.4955091, doi:10.1063/1.4955091.

Jeong, J., Hussain, F., 1995. On the identification of a vortex. Journal of Fluid Mechanics 285, 69–94. doi:10.1017/S0022112095000462.

Lignarolo, L., Mehta, D., Stevens, R., Yilmaz, A., Kuik, G., Andersen, S., Meneveau, C., Ferreira, C., Ragni, D., Meyers, J., van Bussel, G., Holierhoek, J., 2016a. Validation of four LES and a vortex model against stereo-PIV measurements in the near wake of an actuator disc and a wind turbine. Renewable Energy 94, 510–523. doi:10.1016/j.renene.2016.03.070.

Lignarolo, L., Ragni, D., Ferreira, C., van Bussel, G., 2014. Kinetic energy entrainment in wind turbine and actuator disc wakes: An experimental analysis. Journal of Physics: Conference Series 524, 012163. doi:10.1088/1742-6596/524/1/012163.

Lignarolo, L., Ragni, D., Ferreira, C., van Bussel, G., 2016b. Experimental comparison of a wind-turbine and of an actuator-disc near wake. Journal of Renewable and Sustainable Energy 8, 023301. doi:10.1063/1.4941926.

Lumley, J.L., 1967. The structure of inhomogeneous turbulent flows.

Martínez Tossas, L., Churchfield, M., Leonardi, S., 2014. Large eddy simulations of the flow past wind turbines: actuator line and disk modeling. Wind Energy 18. doi:10.1002/we.1747.

Mazellier, N., Vassilicos, J.C., 2010. Turbulence without Richardson–Kolmogorov cascade. Physics of Fluids 22. URL: https://doi.org/10.1063/1.3453708, doi:10.1063/1.3453708.

Medici, D., Ivanell, S., Dahlberg, J.Å., Alfredsson, P.H., 2011. The upstream flow of a wind turbine: Blockage effect. Wind Energy 14, 691 – 697. doi:10.1002/we.451.

Meyer, K.E., Pedersen, J.M., Özcan, O., 2007. A turbulent jet in crossflow analysed with proper orthogonal decomposition. Journal of Fluid Mechanics 583, 199–227. doi:10.1017/S0022112007006143.

Myers, L., Bahaj, A., 2010. Experimental analysis of the flow field around horizontal axis tidal turbines by use of scale mesh disk rotor simulators. Ocean Engineering 37, 218–227. doi:10.1016/j.oceaneng.2009.11.004.

Neunaber, I., 2018. Stochastic investigation of the evolutoon of small-scale turbulence in the wake of a wind turbine exposed to diffeent inflow conditions. Ph.D. thesis. Carl von Ossietzky Universität Oldenburg.

Pierella, F., Sætran, L., 2010. Effect of initial conditions on flow past grids of finite extension. 17th Australasian Fluid Mechanics Conference 2010 .

Porté-Agel, F., Bastankhah, M., Shamsoddin, S., 2019. Wind-turbine and wind-farm flows: A review. Boundary-Layer Meteorology doi:10.1007/s10546-019-00473-0.

Segalini, A., Dahlberg, J.Å., 2020. Blockage effects in wind farms. Wind Energy 23, 120–128. URL: https://onlinelibrary.wiley.com/doi/abs/10.1002/we.2413, doi:10.1002/we.2413.

Sforza, P., Sheerin, P., Smorto, M., 1981. Three-dimensional wakes of simulated wind turbines. Aiaa Journal 19, 1101–1107. doi:10.2514/3.60049.

Siemens, 2019. The socioeconomic impacts of wind energy in the context of the energy transition. https://www.siemensgamesa.com/explore/journal/socioeconomic-report-wind-energy-2019. [Online; accessed 12-December-2019].

Simisiroglou, N., Breton, S., Ivanell, S., 2017. Validation of the actuator disc approach using small-scale model wind turbines. Wind Energy Science 2, 587–601. doi:10.5194/wes-2-587-2017.

Sirovich, L., 1987. Turbulence and the dynamics of coherent structures. i - coherent structures. ii - symmetries and transformations. iii - dynamics and scaling. Quarterly of Applied Mathematics 45. doi:10.1090/qam/910463.

Skeide, A.K., Bardal, L.M., Oggiano, L., Hearst, R.J., 2020. The significant impact of ribs and small-scale roughness on cylinder drag crisis. Journal of Wind Engineering and Industrial Aerodynamics 202. URL: http://www.sciencedirect.com/science/article/pii/S0167610520301021, doi:https://doi.org/10.1016/j.jweia.2020.104192.

Smith, C., Barthelmie, R., Pryor, S., 2013. In situ observations of the influence of large onshore wind farm on near-surface temperature, turbulence intensity, and wind speed profiles. Environmental Research Letters 8. doi:10.1088/1748-9326/8/3/034006.

Stevens, R., Gayme, D., Meneveau, C., 2014. Large eddy simulation studies of the effects of alignment and wind farm length. Journal of Renewable and Sustainable Energy 6. doi:10.1063/1.4869568.

Stevens, R., Meneveau, C., 2014. Temporal structure of aggregate power fluctuations in large-eddy simulations of extended wind-farms. Journal of Renewable and Sustainable Energy 6. doi:10.1063/1.4885114.

Stevens, R., Meneveau, C., 2017. Flow structure and turbulence in wind farms. Annual Review of Fluid Mechanics 49. doi:10.1146/annurev-fluid-010816-060206.

Theunissen, R., Housley, P., Allen, C., Carey, C., 2014. Experimental verification of computational predictions in power generation variation with layout of offshore wind farms. Wind Energy 18. doi:10.1002/we.1788.

Theunissen, R., Worboys, R., 2018. Near-wake observations behind azimuthally perforated disks with varying hole layout and porosity in smooth airstreams at high reynolds numbers. Journal of Fluids Engineering 141. doi:10.1115/1.4041614.

van der Kindere, J., Ganapathisubramani, B., 2018. Effect of length of two-dimensional obstacles on characteristics of separation and reattachment. Journal of Wind Engineering and Industrial Aerodynamics 178, 38 – 48. URL: http://www.sciencedirect.com/science/article/pii/S0167610518300011, doi:https://doi.org/10.1016/j.jweia.2018.04.018.

Veers, P., Dykes, K., Lantz, E., Barth, S., Bottasso, C., Carlson, O., Clifton, A., Green, J., Green, P., Holttinen, H., Laird, D., Lehtomäki, V., Lundquist, J., Manwell, J., Marquis, M., Meneveau, C., Moriarty, P., Munduate, X., Muskulus, M., Wiser, R., 2019. Grand challenges in the science of wind energy. Science , eaau2027doi:10.1126/science.aau2027.

Wu, K.L., Porté-Agel, F., 2017. Flow adjustment inside and around large finite-size wind farms. Energies 10. doi:10.3390/en10122164.

Wu, Y., Porté-Agel, F., 2011. Large-eddy simulation of wind-turbine wakes: Evaluation of turbine parametrisations. Boundary-Layer Meteorology 138. doi:10.1007/s10546-010-9569-x.

Wu, Y., Porté-Agel, F., 2012. Atmospheric turbulence effects on wind-turbine wakes: An LES study. Energies 5, 5340–5362. doi:10.3390/en5125340.

Zhan, L., Letizia, S., Iungo, G., 2019. LiDAR measurements for an onshore wind farm: Wake variability for different incoming wind speeds and atmospheric stability regimes. Wind Energy doi:10.1002/we.2430.

Zhan, L., Letizia, S., Iungo, G., 2020. Wind LiDAR measurements of wind turbine wakes evolving over flat and complex terrains: Ensemble statistics of the velocity field. Journal of Physics: Conference Series 1452. doi:10.1088/1742-6596/1452/1/012077.

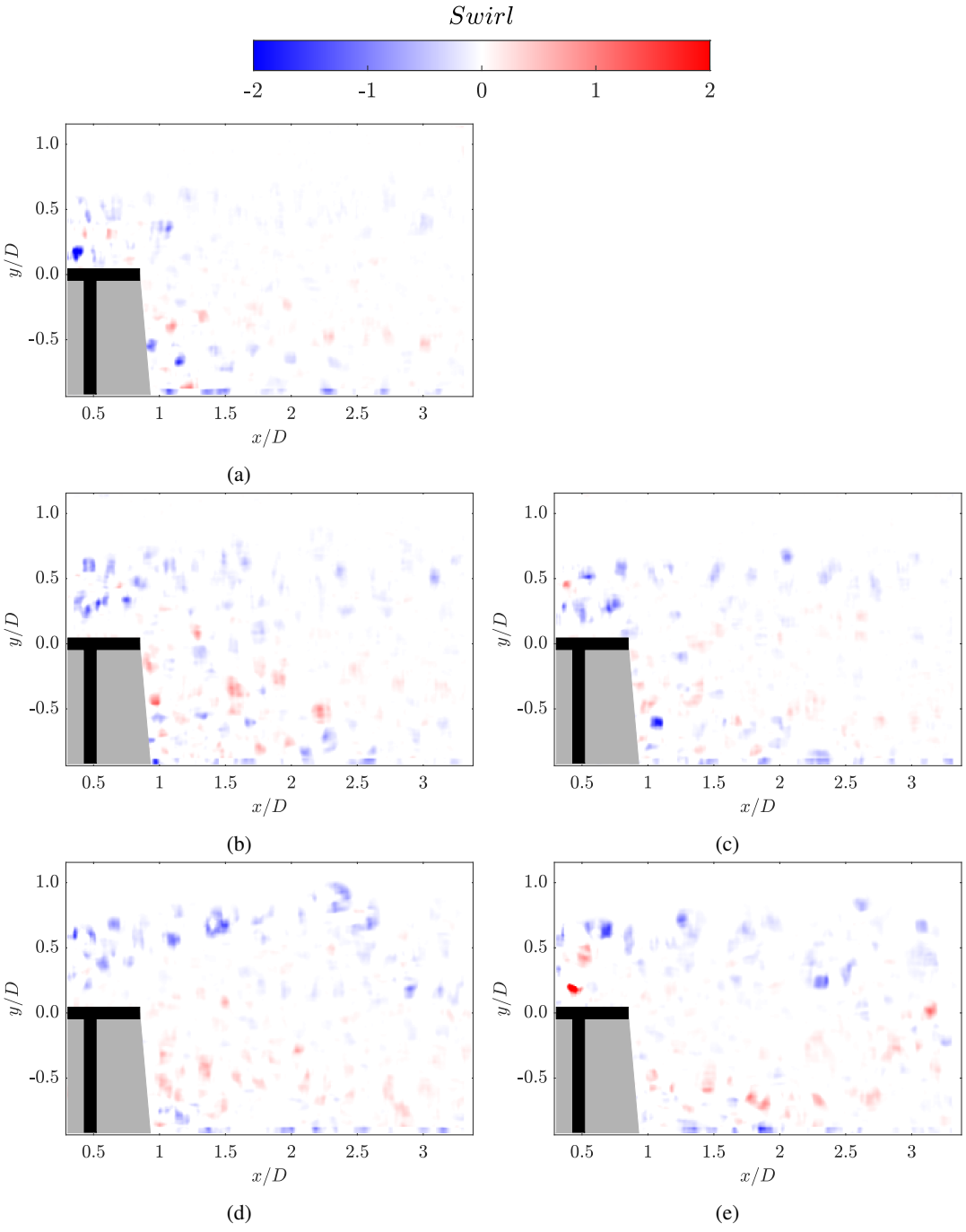

Figure 15: Instantaneous swirling strength signed by vorticity for (a) UHD35, (b) UHD40, (c) NHD40, (d) UHD60 and (e) NHD60. These images are representative of the 1000 PIV measurements that were taken.

A. Flow fields not included in the paper

The swirling strength, turbulence intensity, Reynolds shear stress and POD modes were only showed for the rotating model and NHD35 in this paper. In the following, these characteristics are shown for the UHD35, the disks with 40% solidity and the disks with 60% solidity, as they might be of interest for others that will be working with actuator disks in the future. The solid disk is omitted, due to it only being a reference case.

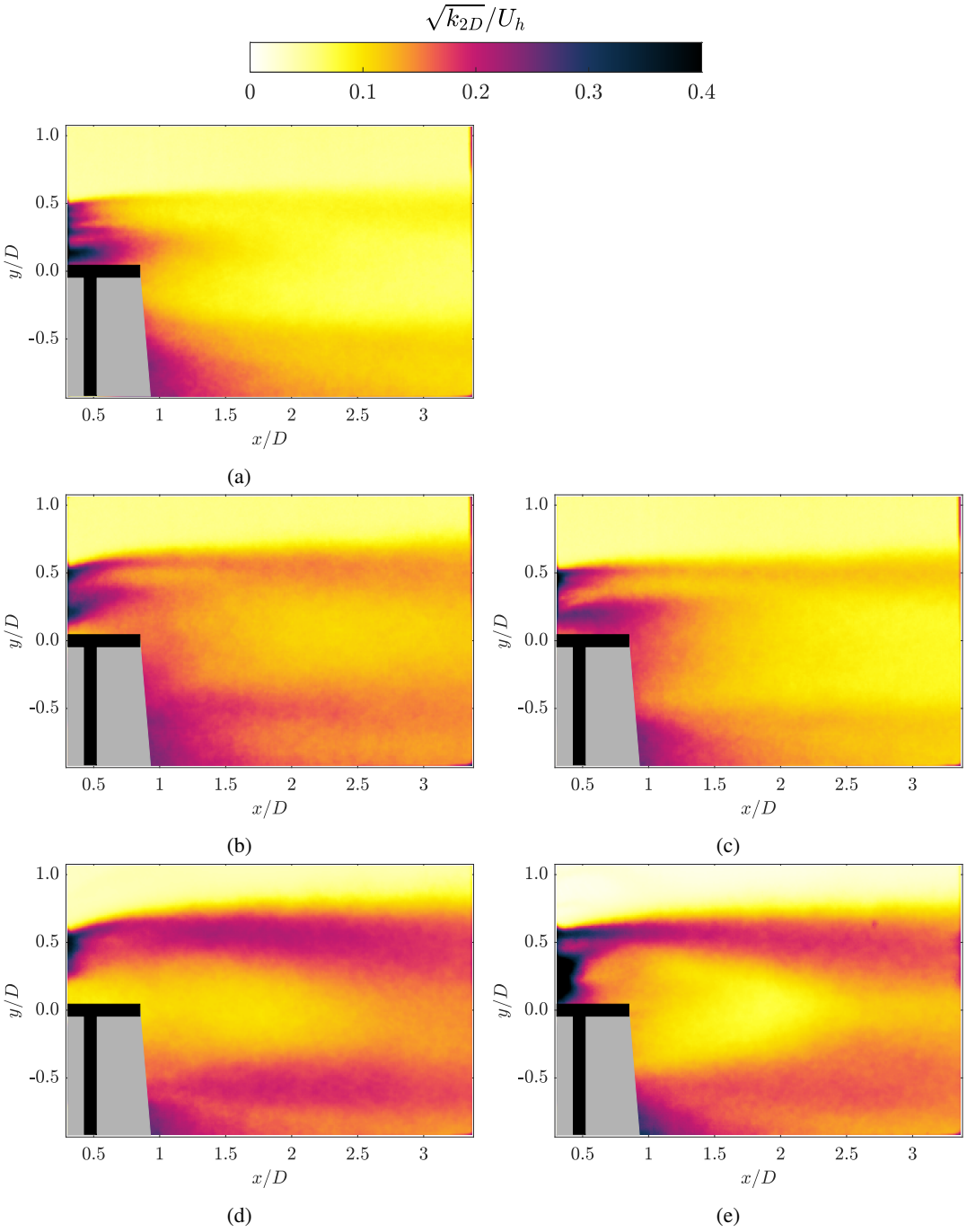

Figure 16: Turbulence intensity fields for (a) UHD35, (b) UHD40, (c) NHD40, (d) UHD60 and (e) NHD60.

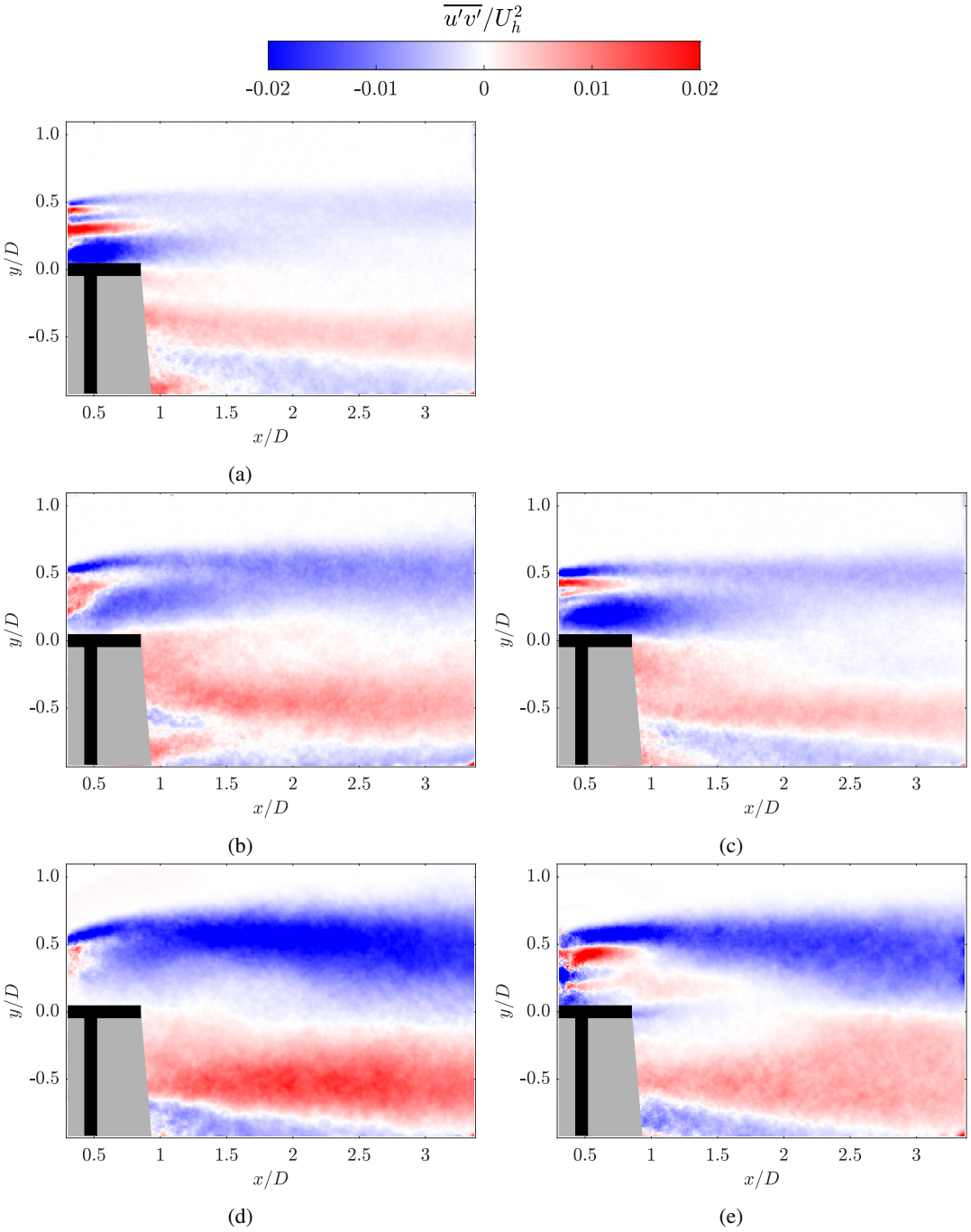

Figure 17: Reynolds shear stress fields for (a) UHD35, (b) UHD40, (c) NHD40, (d) UHD60 and (e) NHD60.

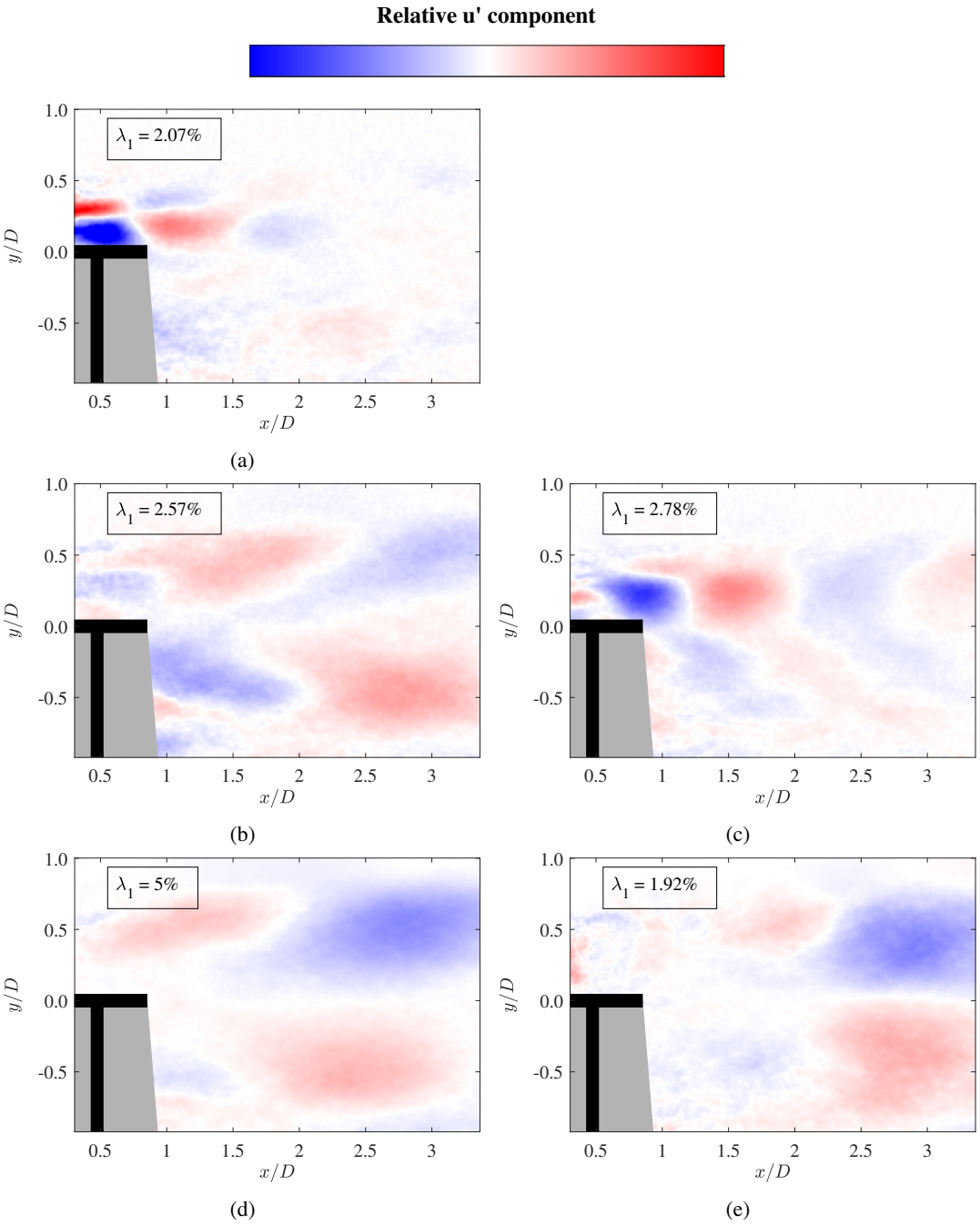

Figure 18: The first u' velocity mode for (a) UHD35, (b) UHD40, (c) NHD40, (d) UHD60 and (e) NHD60.

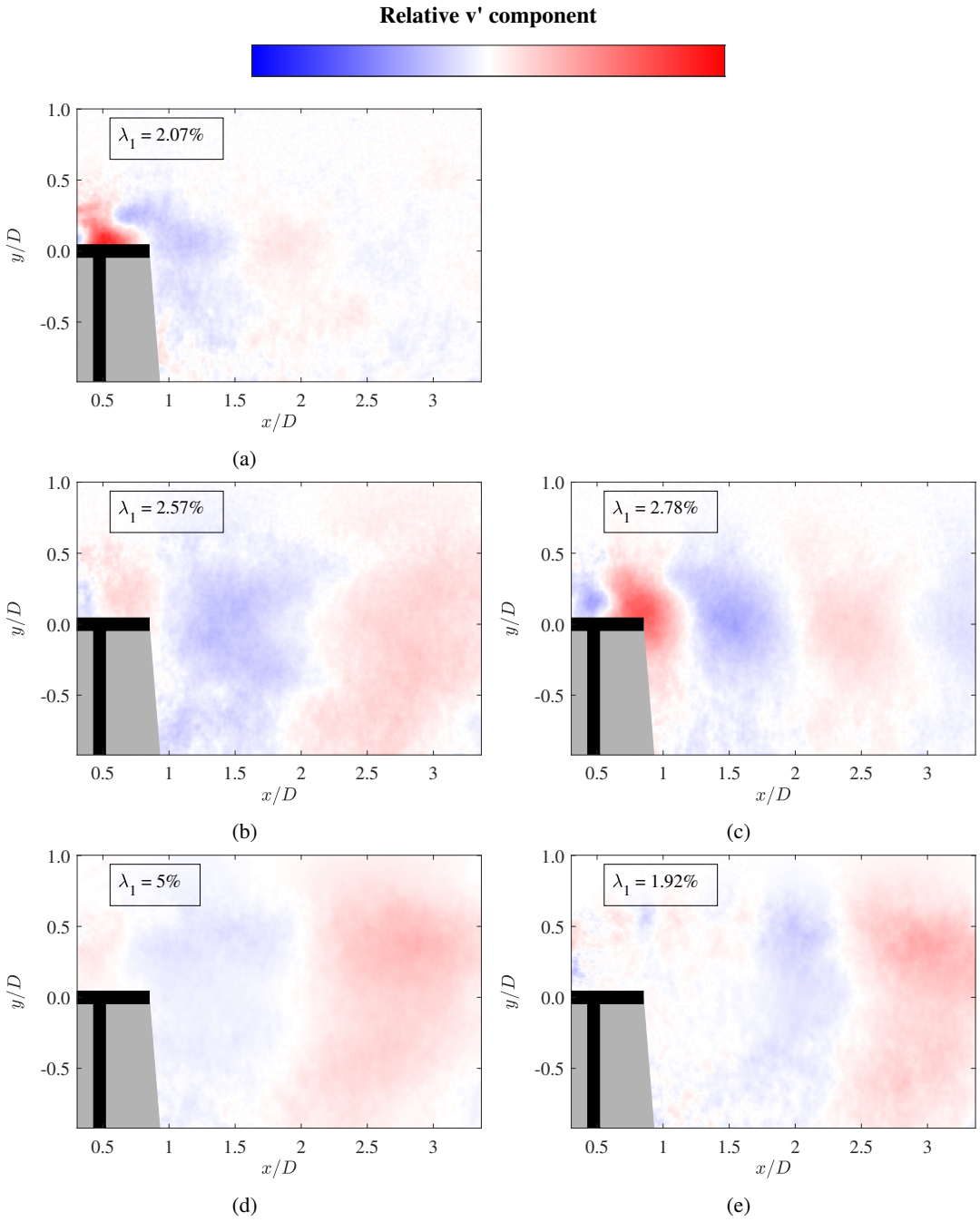

Figure 19: The first v' velocity mode for (a) UHD35, (b) UHD40, (c) NHD40, (d) UHD60 and (e) NHD60.

B. The original project before COVID-19

The objective of this master's thesis had to be changed after two months of work, due to the emerging COVID-19 pandemic that caused the laboratories at NTNU to close down for students on March 12th. This appendix contains a short description of the work done previous to March 12th, and the original plan for the thesis. This appendix is added as a part of the master's thesis for completion, however it will not be a part of the paper that will be submitted to the Journal of Wind Engineering & Industrial Aerodynamics.

The original project concerned the blockage effect produced by the presence of a wind farm, slowing down the incoming flow. This deceleration region immediately upwind of a wind farm is often referred to as the induction zone (Wu and Porté-Agel, 2017), and poses an issue in terms of wind farm planning that has recently gained attention. The individual blockage produced by each wind turbine interacts within a wind farm, so that the velocity field upstream is not only altered locally for a single turbine, but also on the wind farm scale (Forsting and Troldborg, 2015). Branlard (2017) showed, by using a cylindrical vortex wake model and an actuator disk in simulations, that the wind velocity at a distance of 2.5D in front of a wind farm may be reduced by 3% compared to the undisturbed wind velocity at the same location. Hence, the blockage effect has implications for the projected power output from wind farms, as the farms are planned using wind velocity measurements that are conducted without the presence of the not yet build wind farm.

Bleeg et al. (2018) used steady-state RANS simulations of a wind farm, with actuator disks representing the turbines, and compared the results to field measurements conducted at three different wind farms. Both methods showed a slowdown of the wind velocity upstream of the farm. However, the estimate of the magnitude of the slowdown using actuator disk simulations appeared to be inconsistent with the field measurements, and the simulations often underestimated the deceleration. This gives reason to examine the similarities and differences of actuator disks and rotating wind turbines at wind farm scale, focusing on the flow field upstream of the farms, which has often been omitted in previous studies. A deeper understanding of how the flow physics differ is needed to improve the actuator disk model, in order for it to be an accurate tool in physical experiments and in simulations.

This master's project initially aimed at presenting flow field measurements of the upstream effects of wind farms using both rotating wind turbine models and static actuator disks. Drag measurements and PIV measurements of a single rotating model and different actuator disk designs were conducted by the authors at the end of the foregoing semester. At the beginning of the current semester, the PIV flow fields were processed and the data was briefly studied, in order to decide which actuator disk most closely resembled the rotating turbine. This actuator disk and the rotating model was then going to be used to model wind farms. However, after the COVID-19 outbreak causing the laboratories at NTNU to close, the objective of the master's project was changed to concern these already conducted measurements of single turbine models, instead of the not yet finished wind farm measurements.

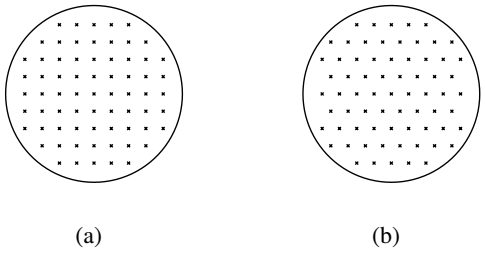

(a) (b)

Figure 20: Illustration of the two wind farm configurations inside the steel disk, (a) being the aligned grid and (b) being the staggered grid.

The original wind farm experiments were to be conducted in a large wind tunnel using PIV. It was decided that the wind farm would be placed on a thin, circular disk in order for the farm to be rotated in-between measurements. The wind tunnel in question has a test section that is 2.7 m wide, and hence, the disk diameter was chosen to be 2.3 m, so that it would easily fit inside the wind tunnel. The disk was made out of magnetic steel. Preliminary tests showed that the disk stayed at rest on the floor of the tunnel without being attached in any way, despite applying high incoming wind velocities. It thus proved to be a suitable mounting platform for the wind farms. After arrival, the disk was polished using methylated spirit, primed and painted matte black.

Two different wind farm layouts had been planned: one aligned grid and one staggered grid. Both were symmetrical and consisted of 69 turbine models. The layouts were optimized as to fit the maximum number of turbines inside the steel disk while maintaining a distance of 5D between both the rows and columns of turbines. Additionally, the farm layouts were made so that the front and the back row of the wind farm consisted of multiple turbines rather than just one, to make sure that the measured blockage effect stemmed from the collection of multiple wind turbine models. The wind farm configurations can be seen in figure 20.

A few more than 69 actuator disks with the chosen design and solidity were 3D printed in PLA, as well as the equivalent number of towers. Magnets were connected at the base of the towers in order to mount them to the steel disk. The towers and the actuator disks were attached to each other and then spray-painted using matte black paint. The rotating turbine models were made at KTH in Stockholm, and had previously been used by Ebenhoch et al. (2017) and Segalini and Dahlberg (2020). KTH provided more than enough rotating models to make the planned wind farm layouts.

Some work had to be done on the wind tunnel itself in order to conduct PIV measurements. The windows in the floor of the wind tunnel were covered using thin plywood boards painted black, which stretched across the whole width of the tunnel. A strip of black duct tape was connected to the front edge of the wooden boards, in order to create a ramp and thus a smoother passage for the incoming flow. A line

of trip tape, designed to trip the incoming flow, was placed at the inlet to the test section. Additionally, an Aluflex bar was adapted to fit at the inlet of the test section, which would be used to change the boundary layer profile of the incoming flow.

A camera stand was built on the outside of the wind tunnel and two LaVision Imager LX 16 megapixel cameras were attached to it. The two cameras would have slightly overlapping fields of view. Most prior studies have focused on the blockage effect of a single turbine, or of an entire wind farm, limited to 2-4D upstream (Medici et al., 2011; Forsting et al., 2016; Branlard, 2017). In this study, the total field of view would be extended to cover the first two rows of wind turbines in the farm as well as 8-10D upstream. The camera stand was covered by a lightproof box, with a small hole for the cameras to look through. The remaining windows on the walls and on the roof of the wind tunnel had been covered using black tarp.

A Litron Nano L200-15 laser, as well as the connected cooling unit, had been placed on top of the wind tunnel roof. A small mirror and a set of optics were chosen and connected to the front of the laser, so that the laser would be reflected down into the tunnel and turn into a thin sheet. The relative placement of the optics had been adjusted so that the laser sheet would have its highest intensity around the hub height of the wind turbine models. A box was created using black painted plywood and black tarp, which was placed on the roof of the wind tunnel. The box was made to enclose the laser, making sure no light escaped, while also having room for someone to sit inside when adjusting the optics prior to the experiments.

When the laboratories were closed on March 12th, there was still some work left to do before the PIV measurements could be conducted. What lacked was to insert the smoke machine into the wind tunnel and adjust the seeding medium and the amount of seeding so that the particles would be detectible for the cameras. The cameras and the camera lenses then had to be focused, and an appropriate frame separation time for the programmable timing unit had to be calculated. These last steps would only have taken a few days. Then, the experiments were set to begin.

According to the original plan, the wind farm measurements were to be conducted with the steel disk rotated to 0, $\pm$14 and $\pm$24.5 degrees. Calculations showed that at each of these angles, one of the turbine models in the front row of the wind farm would be placed in the center of the width of the wind tunnel, meaning this model would be covered by the laser sheet and captured by the cameras. Even though the steel disk would be rotated, the turbine models would always be turned to face the incoming flow, so that the layout of the wind farm would change rather than the angle of the incoming flow relative to the farm. Hence, the blockage effect resulting from multiple wind farm layouts could be determined. The measurements were all going to be conducted at a single wind velocity about 10 m/s, to stay within the Reynolds number independent region while minimizing other detrimental factors such as the models auto-yawing during a test. Two different inflow conditions were to be used: with and without the Aluflex bar changing the incoming flow. Using both the rotating models and the actuator disks, the two incoming flow conditions, the aligned and the staggered grid configuration, and the five different rotations of the steel disk, the resulting measurement data would consist of 40 different cases to be examined.

The PIV measurement data was then supposed to be processed in LaVision Davis 8.4, using the settings from the previous PIV measurements as a starting point when finding a processing method that lead to good correlation values. When the data had been processed, the plan was to study first and second order statistics of the flow fields upstream of the wind farms. Flow characteristics such as velocity, vorticity and Reynolds normal and shear stresses were all to be analyzed. A quantity of added interest would be how far upstream the blockage effect would be noticeable. The main goal of the analysis would be to quantify the similarities and differences between the rotating turbine and the actuator disk in terms of the emerging wind farm blockage effect. Additionally, it would be possible to examine how different wind farm layouts and incoming conditions affected the comparisons.

Due to the laboratories at NTNU closing, the wind farm experiments could unfortunately not be conducted this semester. However, the work that was done will be taken over by a Ph.D. student, who will conduct the wind farm measurements as a part of his Ph.D work once the laboratories open back up. As previously mentioned, it was decided that this master's project would be changed to rather concern the already conducted drag and PIV measurements of single turbine models. Actuator disks are an efficient and common simplification, but the method is still being improved. There is a place for actuator disk studies in the literature, also without using them to model wind farms. In this case, there was the opportunity to show the process of actuator disk selection and to analyze instantaneous phenomena and fundamental flow structures, which have previously gained little attention.

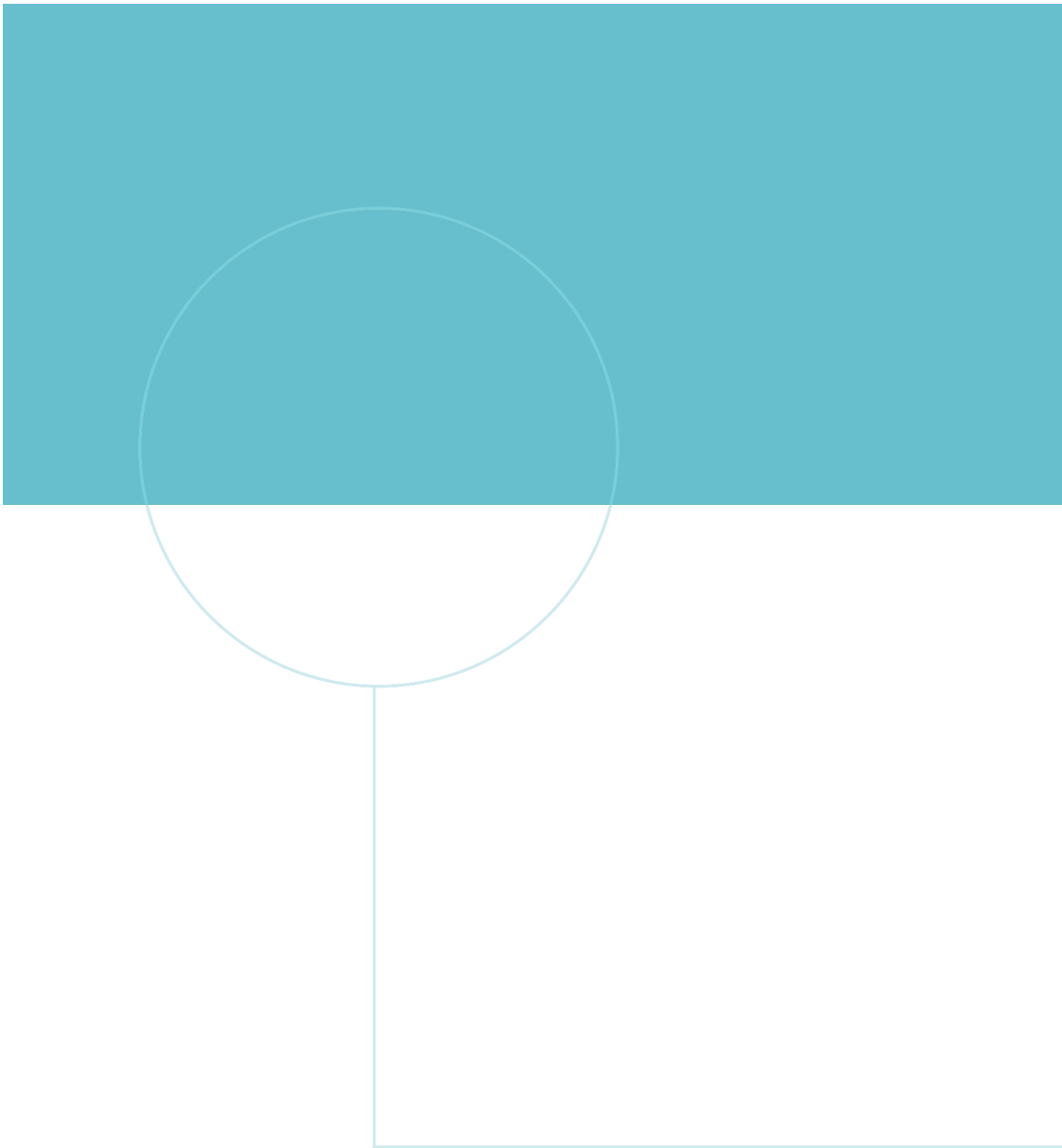

NTNU

Norwegian University of
Science and Technology